SAPIENZA
UNIVERSITÀ DI ROMA

DOTTORATO DI RICERCA IN ENERGIA E AMBIENTE
PhD Program in ENERGY and ENVIRONMENT

36° Cycle

Application of the RSV TAPIRO nuclear research reactor for testing a new neutron cross-section adjustment method

PhD Thesis

Scuola di Dottorato in Scienze e Tecnologie per l'Innovazione Industriale
Facoltà di Ingegneria Civile e Industriale
Dipartimento di Ingegneria Astronautica, Elettrica ed Energetica

Alfonso Santagata

Advisor
Prof. Massimo Corcione

A.A. 2023-2024

Index

1 Introduction

An important aspect of the design of a nuclear system is the reliability of nuclear data. In a Nuclear Reactor, for example, the uncertainties on the neutron cross-sections affect the uncertainties in the evaluation of the cycle length and consequently the number of assemblies. The estimation of the inventory of radionuclides generated by the nuclear reactions, indispensable for defining the radiological hazards expected during the reactor operation and decommissioning, is conditioned by the data uncertainties. In the design of the next generation of fusion experimental facilities and prototype power plants and for defining their maintenance and decommissioning programs, there is a need for accurate knowledge of data related to neutron-induced reactions of materials proposed for regions like vacuum vessel of magnetic confinement fusion tokamaks. The list of applications and fields where the knowledge of “good” nuclear data is not an option is very extensive, in [1] there is a list of international collaborations created to improve nuclear data. The NEA nuclear data High Priority Request List (HPRL) [2] aims to give a guide to measurement and theoretical research groups in focusing their efforts on improving the quality of data for specific cross-sections, primarily of industrial interest. Similar needs have emerged by the US Nuclear Criticality Safety Program (NCSP) [3] that, in its last Five Years Execution Plan [4], enumerates the isotopes and reactions of priority interest for the nuclear applications reporting the laboratories involved in each task and the budget allocated until the year 2028. The Sustainable Nuclear Energy Platform (SNEP), recognized in 2013 as the official European Technology Platform in the nuclear fission sector by the European Commission, has selected the Sodium-cooled Fast Reactor (SFR) and the Lead-cooled Fast Reactor (LFR) as technologies that can achieve the objectives assigned by the Europe in terms of future energy needs with low-carbon technologies. However, the potential effects of nuclear data uncertainties in the reactor design, operation, and safety assessment play an important role when compared with the target accuracy required by researchers, industry, and regulators. The availability of reliable data is then considered a priority in the development of Ge-IV technologies [5].

The incident neutron energy dependence of the cross-section and the energy-angle distributions of the emitted particles can be measured with a dedicated nuclear reactor or accelerator experiments by using different techniques like crystal spectrometers, neutron velocity selectors, and neutron choppers using Time-Of-Flight (TOF) [6]. The use of nuclear reactors as a source of collimated beams extracted utilizing a crystal monochromator or pulsed beams utilizing a mechanical chopper has very much decreased for this kind of measurement, because of competition from accelerator

sources. The n_TOF facility at CERN [7], for example, is able to generate neutrons by reactions occurring in a lead target hit by a pulsed proton beam. The target is conceived to produce neutrons with energy ranging from meV to GeV measured by means of the TOF technique with an energy resolution of $\Delta E/E \approx 10^{-4}$ in the eV region and $\Delta E/E \approx 10^{-3}$ the keV region. These types of experiments are called “differential” because can produce the energy, or even angle, dependence of neutron reactions cross-sections and are generally carried out employing accelerators.

A second type of experiment, called “integral experiments”, provides data that can give indications and previsions on the behavior of the system being designed (target reactor). Enrico Fermi, for example, built many “subcritical piles” that were useful for finding the most optimal material dimension of the “Chicago Pile 1” (CP-1). Experiments, that make use of scale or full-size model of parts of a target reactor (mock-up experiments), allows the determination of parameters of the target reactor by correcting the calculated values with a bias factor [8]. Furthermore, in the design of a mock-up experiment is important to know the representativity factor [9] that “measure” how much the mock-up experiment is representative of the target reactor.

The integral experiments can also be used for measuring quantities (integral quantities) to compare with calculations for testing the reliability of differential cross-sections or adjusting them to reduce the differences. From this point of view, the integral and differential experiments are complementary, if discrepancies between them are observed that means that there exists an inaccuracy in one of them or both. As underlined by Farinelli in [10] the most reasonable and logical approach consists in taking into account all the available information on both differential and integral experiments with appropriate consideration of the characteristics of each type of measurement, accuracies, statistical and possible systematic errors, correlations, normalization and so on (global approach).

The use of existing experimental data or data obtainable with inexpensive new experiments for adjusting the evaluated nuclear data is a possible answer to the request for more reliable nuclear data. This approach requires the utilization of accurate computer simulations and allows the reduction of the need for expensive experimental facilities that can furnish data useful for evaluating some aspects of new systems. The adjusted cross-section methodologies make use of an existing cross-section (*a priori* cross-section) that is corrected to reduce the gap between the estimated uncertainties and the maximum acceptable uncertainties (target accuracies).

The basic concept of the most common adjustment methodologies for correcting the neutron cross-sections, and in general the nuclear data, is described in Chapter 2. A new method, inspired by the adjustment method used for the neutron energy spectrum determination, is proposed in this work and described in Chapter 3. This method aims to overcome the limits and the approximations of the common adjustment methods, like the energy group discretization, the linear approximations, and the compensation effects. The implementation of the proposed cross-section adjustment method is described in Chapters 4 and 5. Chapter 4 exposes the algorithm that performs the correction of a *a priori* cross-section minimizing a cost function with the stochastic hill-climbing optimization method. The use of the Monte Carlo distributions propagation method is proposed for the evaluation of the uncertainties of the adjusted cross-section; this method is described in Chapter 5. A preliminary test of the adjustment method was performed for the adjusting of the radiative neutron capture reaction of the copper isotope ^{63}Cu. The test was based on the available experiment data regarding the neutron activation of copper metallic foils in different positions of two irradiation channels of the RSV TAPIRO research reactor. The RSV TAPIRO reactor, operating at the Casaccia ENEA research center, is briefly described in Chapter 6. Chapter 7 contains the description of the available experimental data, the justification for the selection of the ^{63}Cu(n,γ)^{64}Cu reaction, the algorithm for determining the neutron energy spectra in the experimental positions, the application of the proposed cross-section adjustment method and the results. Future possible tests of the method will require the design and the realization of dedicated experiments to investigate different cross-sections and irradiation positions in the TAPIRO even with the indication reported in Chapter 8. The conclusions and final remarks are in Chapter 9.

2 Cross section adjustment methodologies

Each cross-section adjustment methodology modifies an existing cross-section (*a priori* cross-section) data reducing the discrepancies between calculated and measured values of the quantities measured in integral experiments. The integral quantities can have “global” or “local” characteristics. For example, the critical mass of a nuclear reactor is a global integral quantity because is obtained by an integration performed on the entire volume of the system. The global integral quantities are influenced by several variables, being dependent, in varying degrees, on the properties (material composition, cross-sections, temperatures, etc...) of each point of the system. The count rate of a fission chamber or the spectral indices, on the contrary, are an example of local integral quantity because they are the result of the properties of the fission chamber and the neutron energy distribution in the detector position. In this case, although the neutron energy distribution is a global quantity because depends on the configuration of the entire system or a large portion of it when measured, intervenes in the mathematical formulation of the count rate as a known quantity. The adjustment methodologies can make use of global, local, or both types of integral quantities. The most common neutron cross-section adjustment methodologies are described in [11] where the mathematical formulations on which they are based are compared. As reported in [12], several, adjustment methodologies can be traced back to the minimization of the following cost function:

$$\chi^2_{GLS} = (\boldsymbol{\sigma} - \boldsymbol{\sigma}_m)^t M_\sigma^{-1} (\boldsymbol{\sigma} - \boldsymbol{\sigma}_m) + (\mathbf{E} - \mathbf{C}(\boldsymbol{\sigma}))^t M_E^{-1} (\mathbf{E} - \mathbf{C}(\boldsymbol{\sigma})) \tag{1}$$

where $\mathbf{E}$ is the vector representation of the set of experimental quantities, $\boldsymbol{\sigma}$ is the vector of the multi-group parameters of the model used for calculating the integral quantities, $\mathbf{C}(\boldsymbol{\sigma})$ is the vector of the calculated integral quantities to be compared with $\mathbf{E}$. $\boldsymbol{\sigma}_m$, and M_σ are, respectively, the *a priori* values and covariance matrix of the multi-group parameters, and M_E is the covariance matrix of the experimental data. The parameters are determined by minimizing the cost function (1) that takes into consideration the covariance matrices of experimental and parameters data, for this reason, the method takes the name of the Generalized Least Square (GLS) method. The GLS method, as in the case of the Ordinary Least Square (OLS) method, is valid for linear regression, this is one of the reasons why the $\mathbf{C}(\boldsymbol{\sigma})$ is approximated to the first-order term of the Taylor series:

$$\mathbf{C}(\boldsymbol{\sigma}) \simeq \mathbf{C}(\boldsymbol{\sigma}_m) + S \cdot (\boldsymbol{\sigma} - \boldsymbol{\sigma}_m) \tag{2}$$

where S is the matrix of derivatives $\partial C_i/\partial \sigma_j$, but often it is expressed as the matrix of the relative sensitivity coefficients:

$$S_{ij} = \frac{\delta C_i / C_i}{\delta \sigma_j / \sigma_j} \tag{3}$$

A completely different approach is based on the selection of random cross-section files generated by applying the Total Monte Carlo method to the TALYS code [13]. In this case, the nuclear parameters used by TALYS are sampled by proper probability distributions, generating a set of cross-section files. The optimal cross-section files are those that minimize the differences between the calculated and experimental integral quantities. In this approach, angular and energetic dependence of the cross-sections, average prompt and delayed fission neutron multiplicity, and prompt fission neutron spectrum can be adjusted.

The adjustment methods are based on the agreement between the calculated and experimental values, but compensations can be concealed in the calculation of the integral quantities as highlighted by Farinelli [14] or Salvatores and Palmiotti [15]. In particular, Salvatores and Palmiotti observed that the small total difference between the calculated and experimental values of the effective neutron multiplication factor k_{eff} for the critical assembly JEZEBEL, was the effect of large compensation of the adjustment of different cross-sections. These compensation effects are even more likely, the more the number of different parameters from which the integral quantity depends.

The neutron cross-section adjustment method proposed in this work and described in the next chapter utilizes the local integral quantities defined by the reaction rate of the foils activated by neutrons. This new method depends on the following variables: saturated activities per target nucleus of the irradiated foils, the neutron energy spectra in foils positions, and the *a priori* cross-section to be adjusted.

3 New cross-section adjustment method

The proposed cross-section adjustment method presented in this work takes inspiration from the adjustment methodology used for the determination of the neutron energy distribution (neutron energy spectrum) in the multi-foil activation technique [16, 17]. In this technique, different foils are inserted in a neutron field where radioisotopes are generated by nuclear reactions induced by neutron collisions with the foil nuclei. The radioisotopes are revealed by the decay with the emission of detectable particles like gammas, alphas, electrons, or positrons. The reactions commonly considered are those that generate gamma-emitting radioisotopes whose detection can be made with gamma detectors such as the High Pure Germanium (HPGe) detectors. The measurement of the count rate of specific gamma peaks allows the determination of the reaction rate of the corresponding neutron reactions. The reaction rate R is mathematically connected to the reaction cross-section σ, the number of target nucleus N, and the neutron energy differential flux φ by the relation:

$$R = N \cdot \int_0^\infty \sigma(E) \cdot \varphi(E) dE \tag{4}$$

where N and φ are generally considered time-independent during the irradiation time and the energy integration interval is, in practice, limited to the minimum and the maximum limits of the neutrons' energy. The reaction rate R in relation (4) is the saturated activity and it is common to divided this values by the number of target nuclei, in this case, the relation (4) become:

$$a := R/N = \int_0^\infty \sigma(E) \cdot \varphi(E) dE \tag{5}$$

a is the saturated activity per target nucleus. In the multi-foil technique, foils of different materials are positioned in almost the same position for determining φ at that point. In this case, the reaction rates (saturated activities) of different neutron reactions are measured after the irradiation of the foils in the same neutron energy distribution φ. The discrete number of measured saturated activities per target nucleus a_i^{exp} and the corresponding reaction cross-sections σ_i obtained by one of the different nuclear libraries freely available (IRDFF-II [18], JEFF [19], ENDF [20], JENDL [21], ...) constitute the known quantities in the relation (5) that, for n_R reactions become:

$$\begin{cases} a_i^{calc} & := \int_0^{\infty} \sigma_i(E) \cdot \varphi(E) dE \\ a_i^{exp} & = a_i^{calc} \end{cases} \qquad \forall i = 1, 2, ..., n_R \tag{6}$$

the set of identities $\{a_i^{exp} = a_i^{calc}\}_{i=1,2,...,n_R}$ constitutes the leading condition in the determination of the neutron energy spectrum. The relations (6) represent a system of n_R equations where the unknown quantity is the function φ. As described in paragraph 7.2, exist several methods and computer programs that try to determine the neutron energy differential flux φ from the equations (6) starting from a finite number of reactions n_R. Some of them are based on the correction of a guess neutron energy differential spectrum using correction coefficients that reduce the differences between the calculated and experimental activity values. In this case, the guess energy function is an *a priori* neutron energy differential spectrum that is corrected (adjusted) to minimize the differences between calculation and experiment.

The method proposed for the cross-section adjustment is based on the same basic principle of the neutron spectrum adjustment methods. In the same way as the neutron spectrum adjustment, the *a priori* cross-section is modified to reduce the differences between the calculated and measured values of the saturated activities using the relation (5). In this case, foils of the same type are irradiated in n_P different positions where the neutron spectra are different and well-known. The relation (5) provides the set of equations:

$$a_i = a(\mathbf{r}_i) = \int_0^{\infty} \sigma(E) \cdot \varphi(\mathbf{r}_i, E) dE \qquad \forall i = 1, 2, ..., n_P \tag{7}$$

In the set of equations (7), the known quantities are the saturated activities per target nucleus a_i induced by the reaction under consideration in the foil in position $\mathbf{r}_i$, and the neutron energy differential fluxes $\varphi_i(E) = \varphi(\mathbf{r}_i, E)$ in the same positions. The unknown quantity is the energy-dependent cross-section σ of the considered reaction. In principle, the methods available for the neutron spectrum adjustment could be used for the cross-section adjustment. However, a new algorithm able to provide an energy-continuous solution without inverting matrices and capable of propagating the uncertainties was implemented. Whatever method is chosen, the algorithm that determines the adjusted cross-section $\widetilde{\sigma}$ can be represented as an operator Θ of the measured activities and neutron spectra:

$$\widetilde{\sigma} = \Theta(\sigma_0, \mathbf{a}^{exp}, \boldsymbol{\varphi}) \tag{8}$$

In [8], σ_0 is the *a priori* cross-section function, $\mathbf{a}^{exp}$ is the vector representation of the set of measured saturated activities per target nucleus:

$$\mathbf{a}^{exp} = \{a_1^{exp}, a_2^{exp}, ..., a_{n_P}^{exp}\} \tag{9}$$

and $\boldsymbol{\varphi}$ is the vector function of the neutron energy spectra in the n_P positions:

$$\boldsymbol{\varphi} = \{\varphi_1, \varphi_2, ..., \varphi_{n_P}\} \tag{10}$$

When the uncertainties of both activities and neutron spectra are known, it is possible to determine the uncertainties of the adjusted cross-section $\widetilde{\sigma}$ propagating these uncertainties through Θ. Knowing the probability density functions (pdf) of the activities and neutron energy spectra, considered as random variables, it is possible to determine the pdf of the adjusted cross-section $\widetilde{\sigma}$ from which whatever statistics on $\widetilde{\sigma}(E)$ can be estimated. It should be noted that for the functions φ_i and $\widetilde{\sigma}$ should be known the probability density function of the random variables $\varphi_i(E)$ and $\widetilde{\sigma}(E)$ for each energy E. The reliability of the adjusted cross-section $\widetilde{\sigma}$ depends on the quality, in terms of accuracy and precision, of the activities and neutron energy spectra measurements but also on the adjustment algorithm Θ.

The algorithms proposed for the implementation of the cross-section adjustment method and for the propagation of the uncertainty are described in the following two chapters.

4 The adjustment Algorithm

The optimal adjusted cross-section $\widetilde{\sigma}$ is the energy-dependent function that optimizes a cost function, correcting the *a priori* cross-section σ_0. The cost function quantifies the error between predicted and expected values providing a single real number. Depending on the problem, the cost function can be expressed in many different ways, for the proposed cross-section adjustment method the following formulation is used:

$$\Gamma(\sigma; \mathbf{a}^{exp}, \boldsymbol{\varphi}) = \sum_{i=1}^{n_P} \left(\frac{a_i^{calc}(\sigma, \varphi_i)}{a_i^{exp}} - 1 \right)^2 \tag{11}$$

that is the sum of squares of the relative errors between the calculated and experimental activities in the n_P experimental positions. In relation (11) σ is the function to be optimized, whereas the vector quantities $\mathbf{a}^{exp}$ and $\boldsymbol{\varphi}$, defined in the previous chapter, are considered as constant quantities. $a_i^{calc}(\sigma, \varphi_i)$ is the activity calculated by (7) in position i where the dependence from the cross-section σ and the neutron energy spectrum φ_i are indicated. Then, the (11) can be also written as:

$$\Gamma(\sigma; \mathbf{a}^{exp}, \boldsymbol{\varphi}) = \sum_{i=1}^{n_P} \left(\frac{\int_0^\infty \sigma(E) \cdot \varphi(\mathbf{r}_i, E) dE}{a_i^{exp}} - 1 \right)^2 \tag{12}$$

The function σ that minimizes, in all the experimental positions, the relative differences between the calculated and experimental activities is the searched adjusted cross-section function $\widetilde{\sigma}$. Some constraints must be added in the $\widetilde{\sigma}$ search, the most important is related to the physical definition of cross-section, that is $\widetilde{\sigma}(E) \geq 0$ for all E. The minimization of Γ with the non-negativity constraint can be written as:

$$\widetilde{\sigma} = \underset{\sigma(E) \geq 0 \, \forall E}{\arg\min} \; \Gamma(\sigma; \mathbf{a}^{exp}, \boldsymbol{\varphi}) \tag{13}$$

The function (13) is implemented by the adjustment algorithm Θ mentioned in the previous Chapter, the result of which is assigned to the final optimal function $\widetilde{\sigma}$:

$$\Theta(\sigma_0, \mathbf{a}^{exp}, \boldsymbol{\varphi}) \longrightarrow \widetilde{\sigma} = \underset{\sigma(E) \geq 0 \, \forall E}{\arg\min} \; \Gamma(\sigma; \mathbf{a}^{exp}, \boldsymbol{\varphi}) \tag{14}$$

The minimization algorithm chosen for this work is based on the stochastic Hill-Climbing method [22, 23], a variant of the simple hill-climbing method described in [24]. It is an iterative method where the next vector of parameters (successor) is determined in the steepest uphill direction [25, 26]. In the simple hill-climbing, all the neighbors are examined and the successor in the iterative process is the neighbor that satisfies the optimization conditions. The stochastic hill-climbing variant selects a random neighbor that becomes a successor when it satisfies the optimization conditions, even if it isn't the best successor among the possible neighbors. Figure 1 represents a scheme of the algorithm in its basic form and Figure 2 is an example of a possible path generated by the stochastic hill-climbing algorithm in a maximum search problem for a bivariate function.

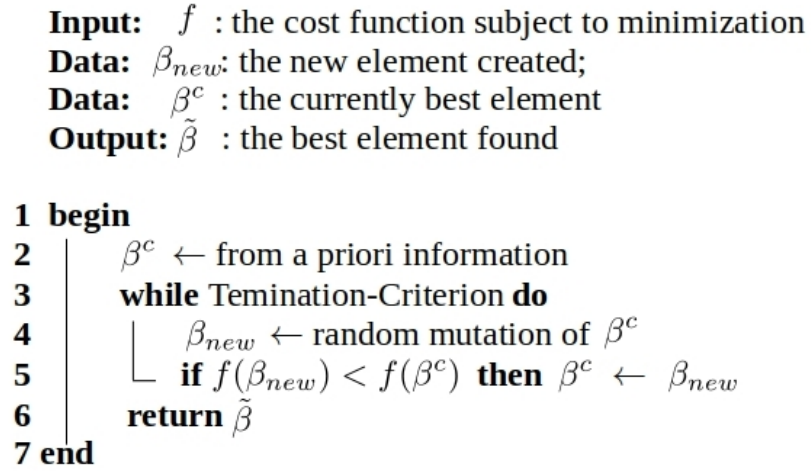

Figure 1: stochastic hill-climbing algorithm for a minimization problem (basic form).

The basic form of the hill-climbing algorithm is not adequate for global optimization but is suitable for the local search. Nevertheless, this limitation doesn't weaken the adjustment procedure but, on the contrary, could provide a credible solution when the *a priori* information is sufficiently reliable because the solution will be close to the *a priori* input.

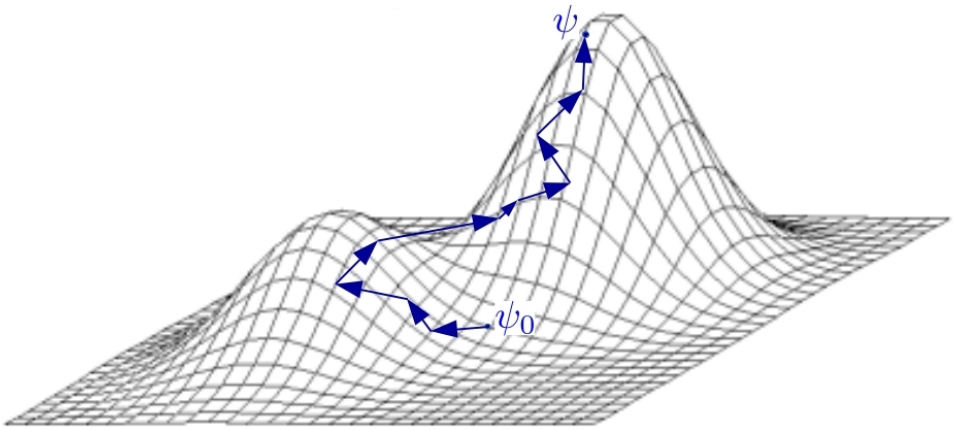

Figure 2: example illustrating a possible path generated by the stochastic hill-climbing algorithm in the search of the maximum of a bivariate function starting from the position ψ_0.

In our case, the optimization refers to minimization of the cost function (11). The application of the stochastic hill-climbing optimization provides an iterative method where starting from the guess function h_0, there is a progressive improvement in the minimization of the cost function by imposing that the function h_{n+1} at step $n+1$ is obtained by the function h_n at step n and the correction function $e^{\gamma_{n+1}}$, such that:

$$h_{n+1} := e^{\gamma_{n+1}} \cdot h_n \text{ with } \Gamma_{n+1} < \Gamma_n \text{ and } n = 0, 1, 2, ... \tag{g}$$

where h_0 is the *a priori* cross-section σ_0 ($h_{n=0} = \sigma_0$), $\Gamma_{n+1} := \Gamma(h_{n+1}; \mathbf{a}^{exp}, \boldsymbol{\varphi})$ is the cost function value at step $n+1$, and $\Gamma_n := \Gamma(h_n; \mathbf{a}^{exp}, \boldsymbol{\varphi})$ is the cost function value at step n. The iterations are stopped when the difference between two consecutive values of the cost function is less than a convergence tolerance value ϵ:

$$|\Gamma_{n+1} - \Gamma_n| < \epsilon \tag{15}$$

The exponent γ_n of the correction function is a continuous function of the neutron energy that was defined as a cubic spline with k knots, then, at the generic step n:

$$\gamma_n := S^{(3)}_{k,n} \tag{16}$$

The spline function $S^{(3)}_{k,n}$ is uniquely defined by the values it assumes in the k knots $E_1, E_2, ..., E_k$:

$$c_{i,n} = S^{(3)}_{k,n}(E_i) \quad \text{for} \quad i = 1, 2, ..., k \tag{17}$$

and the continuity conditions in those points. For the fixed values of the knots, the spline is uniquely defined by the vector $\mathbf{c}_n = (c_{1,n}, c_{2,n}, ..., c_{k,n})$. In the iterative procedure of the Hill-Climbing optimization, the new value of $\mathbf{c}_{n+1}$ is derived by the old vector $\mathbf{c}_n$ with the recursive relation:

$$\mathbf{c}_{n+1} = \mathbf{c}_n + \delta \cdot \mathbf{w} \tag{18}$$

where $\mathbf{w}$ is the direction vector containing k random numbers obtained by sampling the uniform distribution between 0 and 1 and normalized to 1 ($\| \mathbf{w} \| = 1$) and δ is a random number belonging to a uniform distribution between 0 and d ($\delta \sim U(0, d)$), where d is the maximum length that can assumes the step vector $\mathbf{c}_{n+1} - \mathbf{c}_n$ at each iteration ($\| \mathbf{c}_{n+1} - \mathbf{c}_n \| \leq d$). The new vector $\mathbf{c}_{n+1}$ uniquely defines the new spline function $S^{(3)}_{k,n+1}$ and then, the new function h_{n+1}:

$$h_{n+1} = e^{S^{(3)}_{k,n+1}} \cdot h_n \tag{19}$$

The $\mathbf{c}_{n+1}$ will be accepted if the cost function, calculated to the function h_{n+1}, is improved, which means:

$$\Gamma_{n+1} < \Gamma_n \tag{20}$$

The flow chart of the algorithm described in this chapter is shown in Figure 3 and implemented in the GNU Octave high-level language [27] version 5.1.0 installed on the ENEA scientific computing infrastructure CRESCO (Computational RESearch centre on Complex systems) [28]. In the implementation of the optimization algorithm the Mersenne Twister [29] pseudo-random number generator for the sampling of the uniform distribution was used. The energy integration that appears in the definition of the saturated activities per target nucleus $a_i^{calc}(\sigma, \varphi_i)$, see relation (7), was carried out using the numerical doubly-adaptive Clenshaw-Curtis quadrature [30].

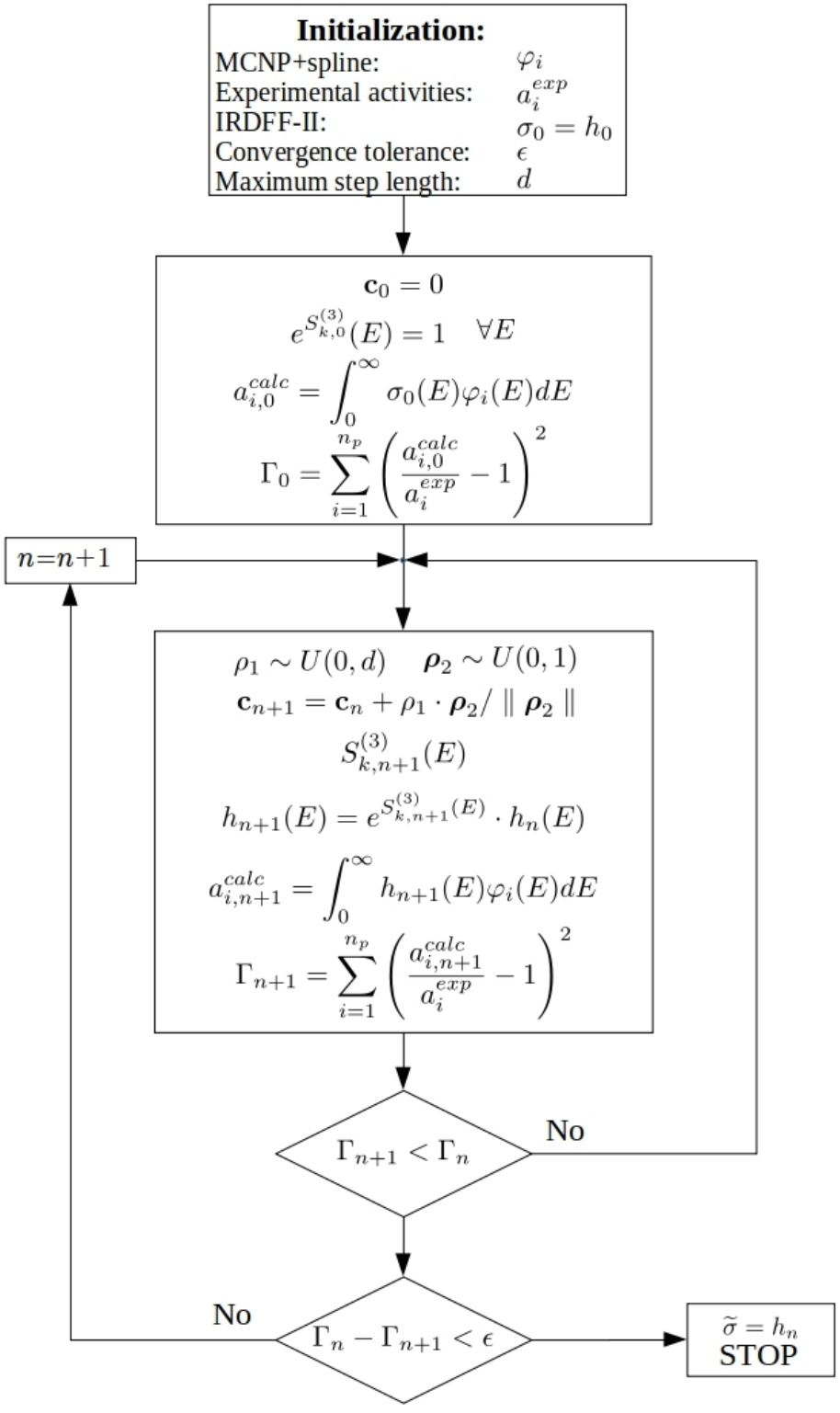

Figure 3: flow chart of the cross-section adjustment algorithm

5 Propagation of Uncertainty

As stated in the previous chapter the adjusted cross-section is derived from the neutron-induced activities per target nucleus, the neutron energy differential spectra in different positions, and the *a priori* cross-section energy-dependent function. When available, the uncertainties of those quantities will affect the final adjusted result which will assumes values according to its probability density function. The propagation of the *a priori* cross-section uncertainties introduces an additional contribution to the total adjusted cross-section uncertainty, attributable to the evaluated nuclear data files. The uncertainties of the *a priori* cross-section, might not be considered if it is meant to propagate only the experimental uncertainties of the quantities measured in the experiment, that is activities and neutron energy spectra.

The application of the method for the propagation of uncertainty based on the second-order approximation of the Taylor series is impractical to the iterative stochastic hill-climbing algorithm, for this reason, the more powerful Monte Carlo technique described in [31] was implemented and included in the adjustment procedure. In this technique, the propagation of uncertainties, or more correctly the propagation of distributions, provides the probability density function of the transformed random variable $\mathbf{Y}$ defined by the map Λ:

$$\mathbf{Y} = \Lambda(\mathbf{X}) \tag{21}$$

where $\mathbf{Y}$ and $\mathbf{X}$ can be multivariate random variables. The probability density function of $\mathbf{Y}$ is obtained by sampling the *pdf* of $\mathbf{X}$ and calculating the corresponding values assumed by the variable $\mathbf{Y}$. The set of values $\mathbf{y}_n = \Lambda(\mathbf{x}_n)$, where $\mathbf{x}_n$ is the value of $\mathbf{X}$ in the nth sampling, constitute a sample of the possible values of the random variable $\mathbf{Y}$ and makes it possible to determine the approximate *pdf*. Increasing the number of samplings (Monte Carlo trials) the approximated probability density function becomes closer to the exact *pdf*. The scheme adopted for the propagation of the uncertainties in the determination of the adjusted cross-section is reported in Figure 4, where the block that performs the adjustment, implements the flow chart of Figure 3.

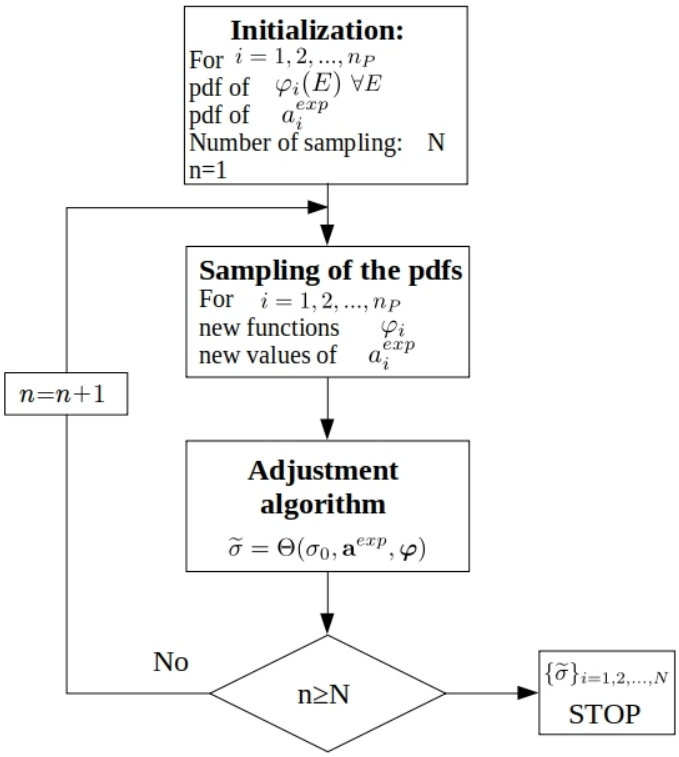

Figure 4: Monte Carlo distribution propagation schema

The *pdfs* of the saturated activities are generally unknown and the unique information available are the mean and the standard deviation of the measured data, in these cases it is assumed that the activities have a normal or log-normal distribution, the latter to prevent having negative values in the sampling of positive quantities. In the case of the neutron energy spectra, which are functions of the neutron energy, the energy differential flux $\varphi_i(E)$ in each experimental position i at the energy E, has a pdf that can be determined by a unfolding or adjusted code able to perform the propagation of uncertainty.

The cross-sections are generally tabulated in the evaluated libraries as points (E_i, σ_i) and for many reactions are available also the standard deviations and the correlation matrix. In the sampling of the cross-section, it is assumed that the random values σ_i have a normal distribution and that each point is independent of the other. This is an approximation that could be removed in future work considering the correlation between those points. However, these correlation were considered negligible in this work. On the other hand, a correlation is still introduced by the cubic spline interpolation of the points (E_i, σ_i) used for having a continuous energy cross-section function.

Changing the name of some variables, the schema of Figure 4 can be adopted for determining the probability density functions of the neutron energy spectra $\boldsymbol{\varphi}$. As described in paragraph 7.2.1, the pdf of the neutron energy spectra, needed for the application of the cross-section adjustment

method to the radiative neutron capture reaction of ^{63}Cu, was determined by an adjustment algorithm similar to that reported in Figure 3. In this case, the algorithm is a function of the *a priori* neutron energy spectrum, the measured saturated activities $\mathbf{a}^{exp} = (a_1^{exp}, a_2^{exp}, ...)$ induced by different nuclear reactions and the relative evaluated cross-sections $\boldsymbol{\sigma} = (\sigma_i, \sigma_2, ...)$:

$$\widetilde{\varphi} = \theta(\varphi_0, \mathbf{a}^{exp}, \boldsymbol{\sigma}) \tag{22}$$

The stochastic hill-climbing optimization method described in the previous paragraph and proposed for the minimization of the cost function, introduces a component in the total uncertainty of the adjusted cross-section originated by the intrinsic stochastic nature of the method. This component was evaluated in the test case and, as reported in paragraph 7.3, it can be considered negligible compared to the other contributions to the total uncertainty.

6 The R.S.V. TAPIRO nuclear research reactor

Figure 5: picture of the TAPIRO reactor hall

Built in the sixties, the zero-power fast research reactor RSV TAPIRO was conceived by the researchers of the Italian National Committee for Nuclear Energy (CNEN) to support the Italian program on fast nuclear reactors. The project was approved in 1965 in the framework of the Italian program RAPTUS (RAPido Torio Uranio Sodio) and 5 and a half years later, on April 2, 1971, TAPIRO provided its first stable neutron flux, reaching its first criticality. In the RAPTUS program were planned the building of small fast reactors and TAPIRO was meant to provide experience on experimental techniques for fast systems, data for shielding predictions, testing of innovative detectors, environment for irradiation biology experiments, etc. [32, 33]. RSV TAPIRO is the Italian acronym of “Reattore Sorgente Veloce TAratura PIla Rapida a potenza 0” and is licensed up to the maximum power of 5 kW which corresponds to a neutron flux in the center of the core of $4 \cdot 10^{12}$ neutrons/cm^2/s. Since the first criticality, the TAPIRO has been used as a source of fast neutrons for several research activities in the fields of aerospace [34], neutron detector test [35], nuclear fusion [36], burning of minor actinides [37], particle accelerators [38], neutron cross-sections testing [39], biological damage [40], etc. Inspired by the concept of the Argonne Fast Source Reactor (AFSR) [41], TAPIRO has a cylindrical core made of several disks assembled in three different stainless still clad, two of them are movable and one, the one on the top, is fixed.

The core is made of highly enriched metallic uranium (weight 98.5% U; 1.5% Mo) surrounded by a cylindrical reflector made of copper. The reflector is divided into two concentric zones: the inner zone, up to 17.4 cm radius, and the outer zone up to 40.0 cm radius, both with a maximum height of 72.0 cm. A 60° sector of the external copper reflector is removable allowing insertion of fissile spectral conversion zones feeding the thermal column. The reactor is surrounded by borate concrete shielding about 170 cm thick.

Many irradiation channels are crossing the reflector. Four experimental channels take place within the system: three different channels at the reactor midplane and one tangential (to the top edge of the core) channel. One midplane channel crosses over the core allowing measures of small samples (internal diameter of the channel in correspondence of the core ≈ 1 cm) in an almost pure ^{235}U neutron fission spectrum. Each channel consists of a metallic cylindrical jacket and a plug for shielding purposes. The plugs are essentially constituted by a stainless-steel casing filled with shielding material for almost the entire section and a copper extension in the area that penetrates the reflector. This extension may be modified for hosting the sample container. The plugs have a gradually reducing section to lower the gamma streaming effect and are provided with three holes available for remote control or power cables eventually needed by the experiments. A large experimental cavity, labeled thermal column (parallelepiped of 110 × 110 × 160 cm^3), is present within the shield zone. Originally, the thermal column was filled with graphite to provide thermal neutrons, but different materials can be placed inside this volume to obtain specific neutron spectra of interest.

The reactor is controlled by several rods made of copper, capable of vertical movement of extraction and insertion inside the inner cylindrical reflector. The insertions of the control rods reduce the neutron leakage and increase the neutron reflection resulting in a positive reactivity insertion. On the contrary, removing the rods the reactivity insertion is negative.

The monitoring is carried out by a proportional counter in the start-up phase and by gamma-compensated ionization chambers at power. In the start-up phase, when the reactor is deeply sub-critical, a minimum amount of neutrons is furnished by an Am-Be neutron source of 185 GBq (5 Ci) that is moved by a mechanism allowing its displacement from the peripheral area of the shield to the core along the radial channel named “Source channel” (see Figure 6a). The experimental channels allow the installation of devices or samples at positions with different neutron fluxes and energy spectra.

Figure 6 shows the horizontal and vertical drawing sections of the TAPIRO and in Table 1, the main characteristics of the TAPIRO are synthetically summarized.

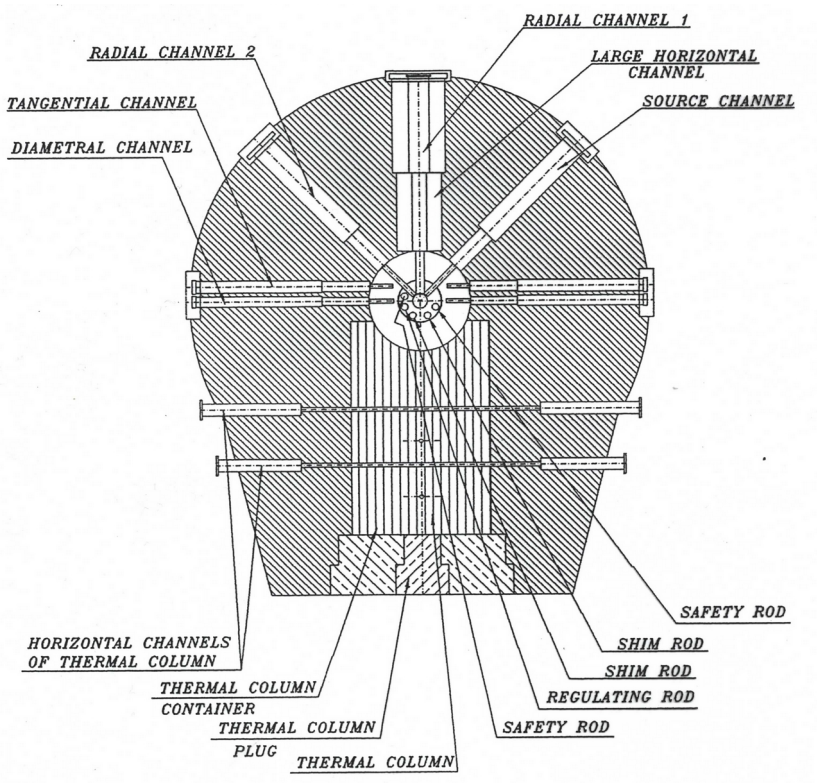

(a)

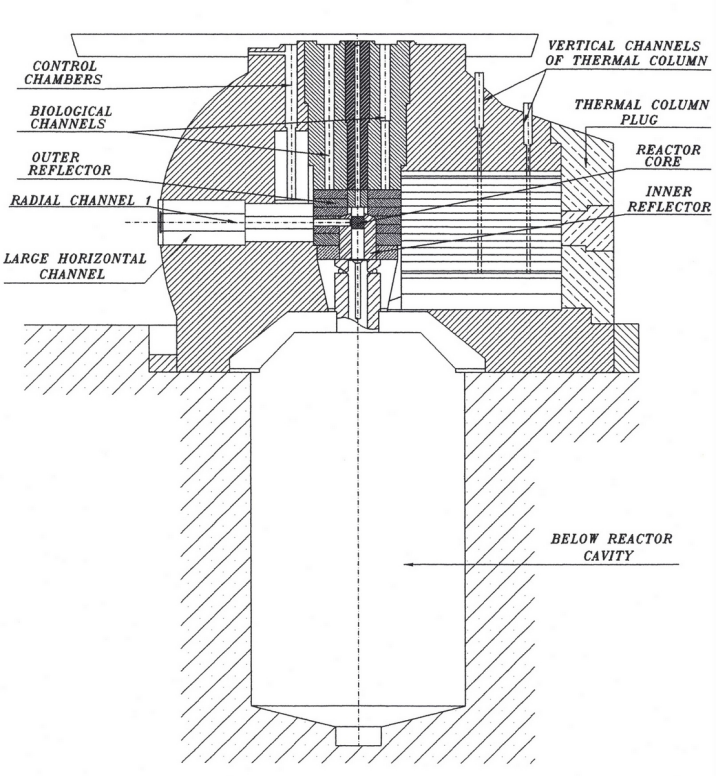

(b)

Figure 6: horizontal (a) and vertical (b) sections of the TAPIRO reactor

The TAPIRO reactor can provide different neutron energy distributions starting from the almost pure fission spectrum in the center of the diametral channel to the epithermal or thermal neutrons in the thermal

column. This variety of neutron energy spectra makes the TAPIRO extremely versatile although it is a zero power reactor. Figure 7 reports some characteristics of the neutron energy distributions provided by the TAPIRO at the maximum power of 5 kW in four distinct positions. The 1 MeV silicon equivalent hardness parameter (see [42] for the definition), the fraction of neutrons with energy higher than 1 MeV, and the average neutron energy indicate the softening of the neutron spectra as the distance from the core center increases. The total neutron flux is $2.9 \cdot 10^{12}$ n/cm^2/s in the diametrical channel and is reduced at $1.1 \cdot 10^{12}$ n/cm^2/s in the innermost position of the thermal column.

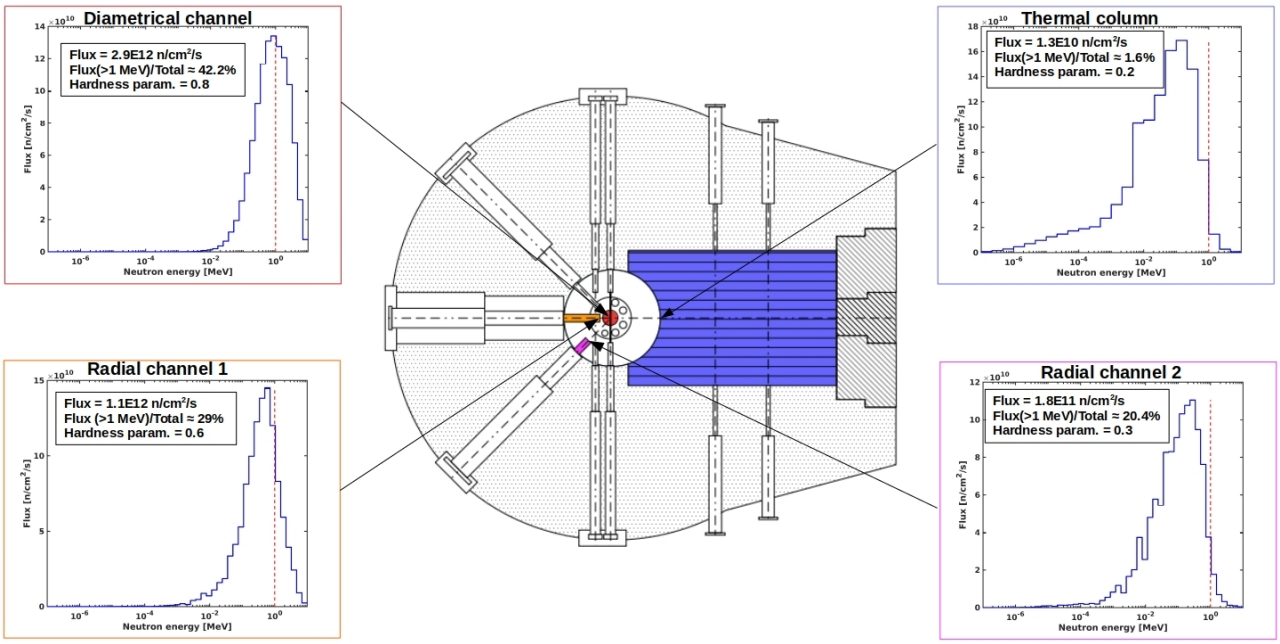

Figure 7: neutron energy spectra (in lethargy unit) in four different positions of the TAPIRO reactor

Table 1: main features of TAPIRO

Description	Data
Maximum steady state power	5 kW
Fuel	Highly enriched uranium Mo-U
Reflector	Copper
Cooling	Helium
Control rods	2 Shim rods + 2 Safety rods + 1 Regulating rod
Maximum neutron flux	$\sim 4.0 \cdot 10^{12}$ n/cm^2/s (experimentally evaluated)
N. of vertical irradiation channels	2
N. of horizontal irradiation channels	4 (2 radial channels + 1 tangential channel + 1 diametral channel) + Thermal Column

7 Application to the ^{63}Cu(n,γ) reaction

As described in paragraph 3 the application of the proposed methodology to a neutron cross-section is based on the selection of several positions in a neutron source system where the neutron energy spectra have different shapes. From the experimental point of view, the realization of the measurement with low uncertainties requires the selection of positions where:

a) the neutron energy spectra are known or measurable with adequate accuracy and precision;

b) the neutron activation induced by the reaction channel under investigation provides a significant reading count rate on the detector for the activity measurement, typically a High Purity Germanium (HPGe) for the detection of gammas.

The achievement of the required level of uncertainty on the adjusted cross-section can be investigated with a feasibility study where the selection of the most suitable measurement positions in the neutron source system, the TAPIRO reactor in our case, must consider the limits of the techniques for the measurement of the neutron energy spectra and activities. The uncertainty of the activity of the radioisotope produced by the reaction under investigation should be as low as the required level of uncertainty.

The preliminary validity of the method was verified by using the available experimental data rather than performing a feasibility study and a dedicated experimental campaign at the TAPIRO reactor. This choice was obligated by the unavailability for bureaucratic reasons of the TAPIRO in the last year. The nuclear reaction and the experimental positions to be used for the preliminary test were then limited to the past experimental data.

The most extensive and systematic experimental work performed at the TAPIRO reactor containing data on neutron activation of metallic foils in different positions of irradiation channels was made by Albert Fabry from 1983 to 1987. Fabry reported in four volumes [43] the results of an Inter-laboratory Consulting Agreement between the Fast Division of the ENEA Casaccia research center and the Reactor Physics Department of the Belgian SCK-CEN laboratory. The primary purpose of those neutronic measurements was the utilization of the results for developing experimental and analytical methods needed to characterize the radiation field in the planned PEC (Prova Elementi di Combustibile - Fuel Elements Test) experimental fast sodium-cooled reactor. The spatial and energetic distribution of neutrons in the TAPIRO were evaluated by means of ^{235}U, ^{238}U, and ^{237}Np fission chambers and passive detectors like Al, Au, Co, In, Ti, and Cu metallic foils. Furthermore, different configurations of control rods and irradiation channel plugs were examined

to evaluate the perturbations on the neutron flux and neutron energy spectra. Although the proposed method could be applied for adjusting the fission cross-section using the count rates measured by fission chambers, for this preliminary test was preferred to use the data provided by the foils. This choice is motivated by the fact that the foil neutron activations were carried out at the same time, with the same control rods and plugs (reflector) configuration, and then the experimental systematic errors and uncertainties were reduced to the minimum.

The examination of the data contained in Frabry's work ended with the choice of the incident neutron energy dependence of $^{63}Cu(n,\gamma)^{64}Cu$ cross-section. This reaction is on the high-priority request list of NEA because of its significant impact on nuclear applications. The Copper is used as a reflector in several critical assemblies and it is inserted into the design of fusion reactors such as ITER. The HPRL request is to improve the cross-section averaged over an incident particle energy spectrum (SIG/SPA) data in the International Reactor Dosimetry and Fusion File (IRDFF) in the fission neutron energy range with an accuracy lower of 2% or 5% [2].

The neutron radiative capture reaction of both ^{63}Cu and ^{65}Cu natural isotopes of copper is of interest also for some particle physics experiments such as those that intend to prove that the neutrino is its antiparticle that, as suggested by Majorana, can be demonstrated by searching the neutrinoless double-β decay [44]. In those experiment, copper is used in the cooling and shielding part of the detector arrangements and the radiation background caused by the neutron-induced reactions could potentially produce signals that are indistinguishable from the signal of interest.

The application of the proposed cross-section adjustment method to the $^{63}Cu(n,\gamma)$ reaction is described in the following paragraphs. The experimental data, extracted from [43], and usable for the application of the cross-section adjustment to the $^{63}Cu(n,\gamma)$ reaction are reported in paragraph 7.1. paragraphs 7.2 and 7.3 describe the processing performed on the experimental data for determining the neutron energy spectra and $^{63}Cu(n,\gamma)$ cross-section adjustment respectively.

7.1. Experimental data

As mentioned in the previous paragraph, the experimental campaign performed by Fabry furnished a set of data related to the neutron activation of Al, Au, Co, In, Ti, and Cu metallic foils for different configurations and power of the TAPIRO reactor [43]. As stated by Fabry, the selected reactions, and then the integral-type sensors, constitute a small but adequate selection of sensors to achieve the purpose of his work.

The data concerning the Cu foils refer to two irradiation runs to which Fabry assigned the names 85/1 and 85/20. In run 85/1, the copper foils were inserted in four positions of the radial channel 1 without another type of foils and reached the power of 100 W. This run was rejected because there is no data to determine the neutron energy spectra. The run 85/20 was performed at 5000 W and the copper foils were inserted in six positions of side B of the tangential channel (TCB) and 2 positions of radial channel 2 (RC2) along with Aluminum and Cobalt foils. Gold, Indium, and Titanium foils were used in different runs and, for this reason, weren't considered in this work.

The usable data are therefore reduced to the activities measured for the foils arranged in the 8 positions of run 85/20. Fabry measured the gamma emission of the radioisotopes produced by the reactions $^{59}Co(n,\gamma)^{60}Co$, $^{27}Al(n,\alpha)^{24}Na$, and $^{63}Cu(n,\gamma)^{64}Cu$ and determined the saturated reaction rates per target nucleus (specific saturated activities) in each experimental position. Table 2 reports the activities measured by Fabry in the positions identified by the field "Position I.D." (fourth column of the table). All the positions are located inside the TAPIRO reflector, as indicated in the Figure 10 of the paragraph 7.2.2. The uncertainties on the measured values are reported in the brackets as a percentage of the relative errors.

As evaluated by Fabry, the geometry and the reactions considered in Table 2 introduce a small perturbation to the local neutron energy distribution and the foils can be treated as infinitely dilute. This means that the self-shielding effects are negligible and the estimation of the corresponding correction factor was unnecessary.

The exact distance of the foils from the core center is reported in Table 3 along with the average values. The maximum distance between the foils located in the same Position I.D. is reported in the last column of Table 3. In all cases, this distance does not exceed the value of 0.051 cm (0.51 mm). In the evaluation carried out in this work, the foils were considered in the average

positions, considering irrelevant the neutron energy spectra variations in two points of the two channels at a relative distance of 0.05 cm.

Table 2: saturated reaction rate per target nucleus

Run I.D.	Power (W)	Channel	Position I.D.	Reaction rate per target nucleus (1/s)		
				63Cu(n,γ)	59Co(n,γ)	27Al(n,α)
85/20	5000	TCB	P1	1.5415E-14 (0.5%)	2.0411E-14 (0.5%)	2.9733E-17 (0.5%)
			P2	1.3281E-14 (0.5%)	2.0353E-14 (0.5%)	9.6969E-18 (0.5%)
			P3	1.1250E-14 (0.5%)	2.0470E-14 (0.5%)	4.0118E-18 (0.5%)
			P4	8.9884E-15 (0.5%)	1.9151E-14 (0.5%)	1.4461E-18 (0.5%)
			P5	6.4518E-15 (0.5%)	1.6969E-14 (0.5%)	5.9136E-19 (0.5%)
			P6	4.6797E-15 (0.5%)	1.6290E-14 (0.5%)	3.1740E-19 (0.6%)
85/20	5000	RC2	P1	5.4730E-15 (0.5%)	1.5956E-14 (0.5%)	3.3488E-19 (0.4%)
			P2	3.8033E-15 (0.5%)	1.4452E-14 (0.5%)	1.8511E-19 (0.4%)

Table 3: foils distance from the core center

Channel	Position I.D.	Distance from the core center (cm)				
		Cu foil	Co foil	Al foil	average	Maximum difference
TC/B	P1	11.755	11.750	11.760	11.755	0.020
	P2	13.117	13.120	13.145	13.127	0.028
	P3	16.000	16.010	16.040	16.017	0.040
	P4	19.745	19.750	19.790	19.762	0.045
	P5	23.953	23.960	24.000	23.971	0.047
	P6	28.419	28.430	28.470	28.440	0.051
RC2	P1	26.340	26.340	26.390	26.357	0.050
	P2	31.340	31.340	31.390	31.357	0.050

The data reported in Tables 2 and 3 are of fundamental importance in the application of the proposed cross-section adjustment method at the ^{63}Cu(n,γ) reaction. As reported in the following paragraphs, the neutron energy distributions, estimated by a neutron transport code in the average positions of Table 3, were corrected using the measured activities of the reactions ^{59}Co(n,γ) and ^{27}Al(n,α) of Table 2. Finally, the IRDFF-II evaluated cross-section of the reaction ^{63}Cu(n,γ) was adjusted reducing the differences between the experimental values reported in the fifth column of Table 2 and those calculated with the corrected neutron energy spectra. The propagation of the uncertainties of the measure activities and evaluated cross-sections was performed with the algorithm described in Chapter 5.

7.2. Neutron energy spectra in the experimental positions

The measurement of the neutron energy spectrum at a point inside a neutron field can be performed with several methods, some are applicable over a wide energy range, and others can only used in certain ranges of energy [45]. The common method used in a research reactor is based on the analysis of activation induced by neutrons in a detector specimen [46]. As introduced in paragraph 3 the multi-foil activation technique is based on the measurement of activities of radioisotopes generated by specific nuclear reactions between neutrons and specimen's nuclei. The neutron energy spectrum is determined by the measured activities and a computer program that can "unfold" the equations that constitute the mathematical formulations of the problem or adjust a guess (*a priori*) neutron energy spectrum. The measured activities and the corresponding evaluated cross-sections (JEFF, ENDF, JENDL, ...) are the main ingredients of each unfolding or adjustment computer program.

A proper application of the multi-foil activation technique requires the measurement of activities induced by a sufficient set of neutron reactions. Unfortunately, the data available in Table 2 for the application of the multi-foil techniques are reduced to the two reactions $^{59}Co(n,\gamma)^{60}Co$ and $^{27}Al(n,\alpha)^{24}Na$. With only two reactions it is easy to reach an excellent agreement between the calculated and experimental values, although the adjusted neutron energy spectrum could be affected by inaccuracy. This deficiency is partially attenuated by the circumstance that the two available reactions cover the two typology of sensors, the non-threshold sensors covered by the $^{59}Co(n,\gamma)$ reaction and the threshold sensors covered by the $^{27}Al(n,\alpha)$ reaction. The availability of a validated computer model of the TAPIRO, that ensures, in some measure, the reliability of the *a priori* neutron energy spectra, is a further condition that alleviates the poorness of usable reactions. Furthermore, this chapter intends to provide a preliminary test on the applicability of the proposed cross-section adjustment method rather than gives definitive results on the method itself or on whatever cross-section adjustment. However, a list of possible reactions for the application of the multi-foil activation technique in TAPIRO, which should include at least the reactions considered by Fabry, is reported in Chapter 8. After these preliminary considerations, the next paragraphs report the description of the method adopted for the neutron energy spectra determination and the relative results, including the propagation of uncertainties.

7.2.1 Neutron energy spectra adjustment

Several unfolding and adjustment codes are based on the optimization, generally a minimization, of a cost function that has the aim of reducing the differences between the calculated and measured saturated activities per target nucleus. Codes like STAY'SL [47], LEPRICON [48], DIFBAS [49], and DIFMAZ [50] use the linear least-square method for minimizing the cost function, others, like SAND-II [51, 52], LOUHI [53] and GRAVEL [50] the non-linear least-square method. Some of them, like SAND-II, respect the non-negativity of the neutron energy distribution, and others, like STAY'SL, can generate solutions that may have negative values in some energy groups. In addition to these traditional codes, based on the so-called minimal least-square methods, there are codes based on the Bayesian theory and maximizing an entropy function obtained by the Lagrange method [54]. An overview of the most common unfolding techniques is in [16] and [17]. As mentioned in paragraph 3 the starting point for each unfolding or adjustment procedure is the system of equations:

$$a_i^{exp} \approx a_i^{calc} = \int_0^{\infty} \sigma_i(E) \cdot \varphi(E) dE \quad \forall i = 1, 2, ..., n_R \tag{23}$$

where the relations $a_i^{exp} \approx a_i^{calc}$ for all the n_R reactions mean that the values a_i^{exp} and a_i^{calc} are, at the end of the minimization, approximately equal. The ill-posedness of the equations (23) justifies the proliferation of codes that use those equations in the attempt to extract the function φ with as much detail as possible from a finite number of measured values a_i^{exp}. The lack of a unique solution can be solved by adding *a priori* physical information and a cost function, but the choice of the *a priori* information and the cost function is almost arbitrary. The method adopted in this work is based on the non-negativity condition and a reliable guess neutron energy spectrum combined with a revised cost function.

The natural choice for the cost function is the residual sum of square:

$$\Gamma(\varphi) = \sum_{i=1}^{n_R} (a_i^{calc}(\varphi) - a_i^{exp})^2 \tag{24}$$

between the calculated a_i^{calc} and experimental a_i^{exp} values of saturated activities per target nucleus caused by the n_R reactions. The minimization of the functional $\Gamma(\varphi)$ provides the optimal differential neutron spectrum function $\widetilde{\varphi}$:

$$\widetilde{\varphi} = \underset{\varphi(E)\geq 0\,\forall E}{\arg\min}\ \Gamma(\varphi) \tag{25}$$

In (25) only the non-negativity constraint is considered, but further conditions can be included in the optimization by adding additional terms to the definition of the cost function (24). The numerical solution of the relation (25) can be affected by the differences between the saturated activities that, depending on the reaction cross-sections, in some cases can differ greatly from each other. For example, if for a reaction l we have $a_l \gg a_i\,\forall i \neq l$ there is the possibility that the sum in (24) is reduced at a single term: $\Gamma \simeq (a_l^{calc} - a_l^{exp})^2$. In this extreme case, reaction l prevails over the others and the numerical minimization is mainly performed with respect to that reaction, being the other terms of (24) negligible even if the relative error of some of those terms could be large. One solution to this problem is weighting the residuals in (24) with a suitable coefficients w_i that makes each term of the sum balanced: $\Gamma(\varphi) = \sum w_i \cdot (a_i^{calc}(\varphi) - a_i^{exp})^2$. The solution adopted in this work starts from the consideration that the differential neutron spectrum function φ can be written as the product between the total flux Φ and an energy-dependent function g:

$$\varphi(E) := \Phi \cdot g(E) \quad \forall E \tag{26}$$

where

$$\Phi := \int_0^\infty \varphi(E)dE \tag{27}$$

and the shape function g is normalized to unity:

$$\int_0^\infty g(E)dE = 1 \tag{28}$$

In the approximation that each foil is invested by the same neutron field, the total flux can be determined by substituting the (26) in (23):

$$\Phi = \frac{a_i^{calc}}{\int_0^\infty \sigma_i(E) \cdot g(E)dE} \tag{29}$$

The relation (29) is mathematically true for each reaction i but, substituting the calculated activities a_i^{calc} with the experimental values a_i^{exp}, the total flux will differ for each reaction:

$$\Phi_i = \frac{a_i^{exp}}{\int_0^\infty \sigma_i(E)\cdot g(E)dE} \qquad \text{for} \qquad i = 1, 2, ..., n_R \tag{30}$$

Since the fluxes Φ_i are evaluated in the same (approximately the same) point the unbiased variance S^2

$$S^2(\Phi) = \frac{1}{n_R - 1}\sum_{i=1}^{n_R}(\Phi_i - \overline{\Phi})^2 \qquad \text{with} \qquad \overline{\Phi} = \frac{1}{n_R}\sum_{i=1}^{n_R}\Phi_i \tag{31}$$

or equivalently, the quantity:

$$(n_R - 1)\cdot\frac{S^2(\Phi)}{\overline{\Phi}} = \sum_{i=1}^{n_R}\left(\frac{\Phi_i}{\overline{\Phi}} - 1\right)^2 \quad \text{if } \overline{\Phi} \neq 0 \tag{32}$$

should be almost zero. Considering that Φ_i and $\overline{\Phi}$ are functions dependent on g, the (32) become:

$$(n_R - 1)\cdot\frac{S^2(\Phi(g))}{\overline{\Phi}(g)} = \sum_{i=1}^{n_R}\left(\frac{\Phi_i(g)}{\overline{\Phi}(g)} - 1\right)^2 \tag{33}$$

The relation (33) was used as cost function and the optimal $\widetilde{g}$ was determined by:

$$\widetilde{g} := \underset{g(E)\geq 0\,\forall E}{\arg\min}\ \Gamma^{rev}(g) \tag{34}$$

where

$$\boxed{\Gamma^{rev} := \sum_{i=1}^{n_R}\left(\frac{\Phi_i(g)}{\overline{\Phi}(g)} - 1\right)^2} \tag{35}$$

is the revised cost function. Γ^{rev} is nonlinear, doesn't depend on the total flux Φ, and its minimization provides only the optimal energy shape function $\widetilde{g}$ whereas the optimal value of the total flux $\widetilde{\Phi}$ is the mean:

$$\widetilde{\Phi} := \frac{1}{n_R}\sum_{i=1}^{n_R}\widetilde{\Phi}_i = \frac{1}{n_R}\sum_{i=1}^{n_R}\frac{a_i^{exp}}{\int_0^\infty \sigma_i(E)\cdot\widetilde{g}(E)dE} \tag{36}$$

where

$$\widetilde{\Phi}_i := \frac{a_i^{exp}}{\int_0^\infty \sigma_i(E)\cdot\widetilde{g}(E)dE} \quad \text{for} \quad i=1,2,...,n_R \tag{37}$$

are the optimal total fluxes per each reaction. The final neutron energy differential spectrum is the product of the two terms:

$$\widetilde{\varphi}(E) = \widetilde{\Phi}\cdot\widetilde{g}(E) = \left[\frac{1}{n_R}\sum_{i=1}^{n_R}\frac{a_i^{exp}}{\int_0^\infty \sigma_i(E)\cdot\widetilde{g}(E)dE}\right]\cdot\left[\underset{g(E)\geq 0\,\forall E}{\arg\min}\ \Gamma(g)\right] \quad \forall E \tag{38}$$

Furthermore, the best estimation of the calculated activities per target nucleus are:

$$\widetilde{a}_i^{calc} = \widetilde{\Phi}\cdot\int_o^\infty \sigma_i(E)\cdot\widetilde{g}(E)dE \quad \text{for} \quad i=1,2,...,n_R \tag{39}$$

It is possible to prove that the minimization of (24) corresponds to the minimization of the residual sum of the square of the activities $\sum(a_i^{calc}(\varphi)-a_i^{exp})^2$. The minimization is an iterative process where the best value of the calculated activities at each iteration is obtained by the average values of the total flux $\overline{\Phi}$:

$$a_i^{calc}(\varphi) = \overline{\Phi}\cdot\int_0^\infty \sigma_i(E)\cdot g(E)dE \quad \text{where} \quad \varphi=\Phi\cdot g \tag{40}$$

At each minimization iteration, the average flux $\overline{\Phi}$ can be determined by the relation (40) and the fluxes per reaction Φ_i from (30), then:

$$\left|\frac{\Phi_i}{\overline{\Phi}}-1\right| = \left|\frac{a_i^{exp}/\int_0^\infty \sigma_i(E)g(E)dE}{a_i^{calc}(\varphi)/\int_0^\infty \sigma_i(E)g(E)dE}-1\right| = \left|\frac{a_i^{exp}}{a_i^{calc}(\varphi)}-1\right| = \frac{\left|a_i^{exp}-a_i^{calc}(\varphi)\right|}{a_i^{calc}(\varphi)} \tag{41}$$

The last identity of (41) proves that minimizing the residuals $\left|\Phi_i/\overline{\Phi}-1\right|$ involves the minimization of the residuals $\left|a_i^{exp}-a_i^{calc}\right|$ of the sum $\sum(a_i^{calc}(\varphi)-a_i^{exp})^2$ that will therefore be minimized.

Furthermore, the identities (41) establish that the revised cost function is equivalently defined by the sum of squares of relative differences between the activities, that is to say:

$$\Gamma^{rev} = \sum_{i=1}^{n_R}\left(\frac{\Phi_i(g)}{\overline{\Phi}(g)}-1\right)^2 = \sum_{i=1}^{n_R}\left(\frac{a_i^{exp}}{a_i^{calc}(\varphi)}-1\right)^2 \tag{42}$$

The minimization function $\widetilde{g} = \underset{g(E)\geq 0\,\forall E}{\arg\min}\ \Gamma^{rev}(g)$ of the revised cost function (35) was reached by applying the stochastic hill-climbing algorithm describer in Chapter 4. The fulfillment of the non-negativity condition and the introduction of the initial neutron energy spectrum were instead accomplished by means of the definition:

$$\widetilde{g}(E) = \frac{1}{\alpha} \cdot e^{\gamma(E)} g_0(E) \tag{43}$$

where γ is a function that can also assumes negative values, g_0 is the shape function of the *a priori* neutron energy spectrum and α is the coefficient that normalizes $\widetilde{g}$:

$$\alpha := \int_0^\infty e^{\gamma(E)} g_0(E) dE \tag{44}$$

The progressive correction of the guess neutron energy spectrum was realized by the recursion:

$$g_{n+1}(E) = \frac{1}{\alpha_{n+1}} \cdot e^{\gamma_{n+1}(E)} g_n(E) \qquad \text{such that} \qquad \Gamma^{rev}_{n+1} < \Gamma^{rev}_n \tag{45}$$

and the final result $\widetilde{g}$ was obtained when the convergence criterion was reached. For example when the difference between two consecutive values of the cost function is lower than a convergence tolerance ϵ, according to relation (15).

By what was reported in Chapter 4, the exponent of the correction function was approximated with the continuous cubic spline:

$$\gamma_n(E) \simeq S^{(3)}_{k,n}(E) \qquad \forall E \tag{46}$$

The iterative scheme, similar to that defined for the cross-section adjustment in Figure 3, is represented in Figure 8 where are reported the main relations responsible for the optimization process.

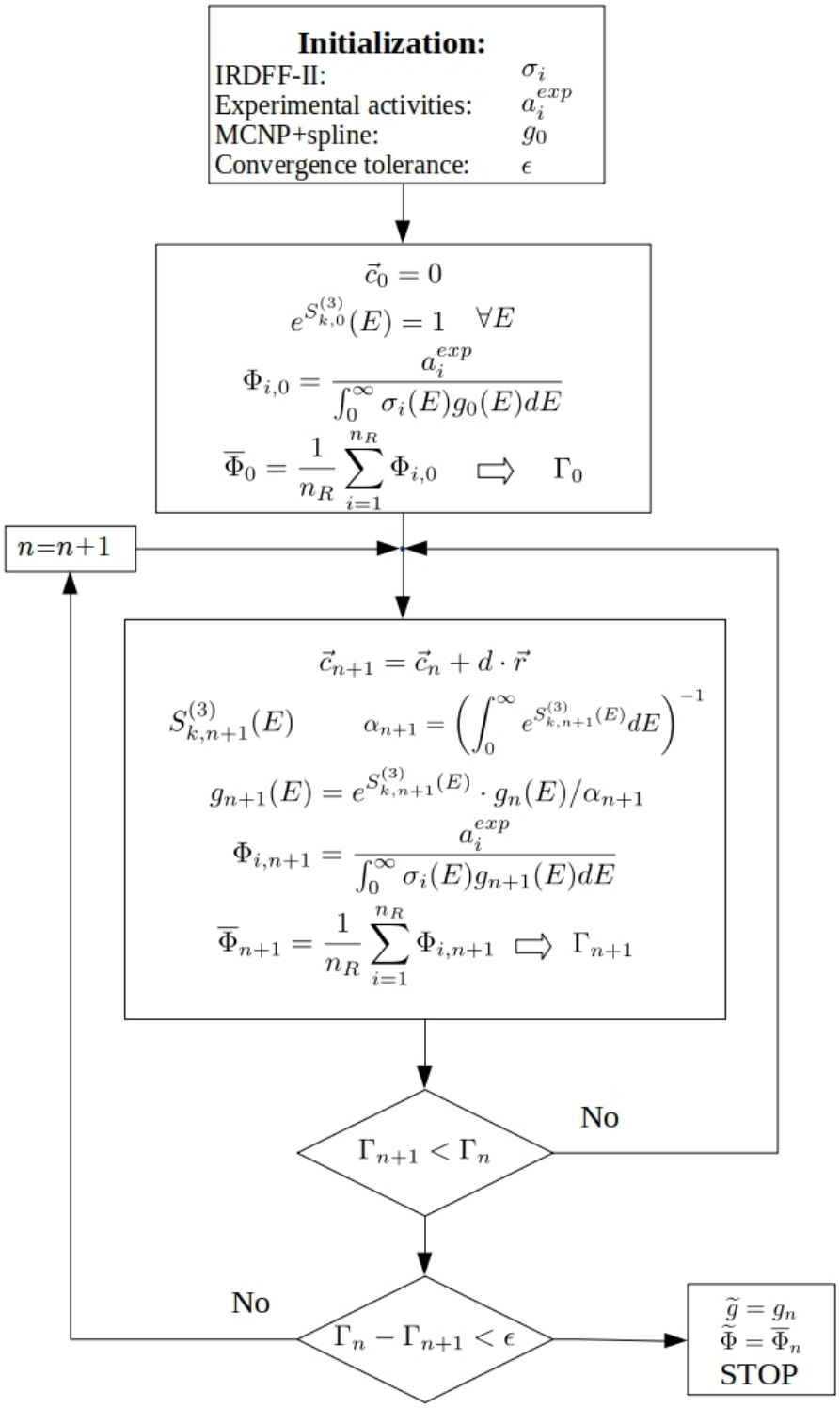

Figure 8: iterative scheme for the neutron energy spectrum adjustment

7.2.2 MCNP model of TAPIRO reactor and the *a priori* neutron energy spectra

The initial neutron spectrum required by the adjustment procedure is of fundamental importance for at least two reasons. The first is that starting with a first attempt function close to the final result, the algorithm will converge more rapidly. The second, and more important reason, is that starting from a neutron spectrum that doesn't take into adequate account the real experimental conditions, the algorithm could converge to a neutron energy spectrum that reproduces perfectly the experimental data but that is far from the real spectrum. For these reasons, the simulated *a priori* spectrum must be the result of a certified neutron transport code, reliable nuclear data, and a validated model as possible adherent to the experimental configuration. The neutron energy distributions for the adjustment were estimated with the MCNP code version 6.2 [55] and a model of TAPIRO validated in 2014 as reported in [56]. The model was validated with version 2.7.0 of the Monte Carlo transport code MCNPX comparing the results obtained with the experimental data about the nominal count rates provided by ^{235}U, ^{238}U, ^{237}Np, and ^{239}Pu fission chambers irradiated at different distances from the core center [43]. Both ENDF/B-VII and JEFF 3.1 neutron cross-section were used in the validation of 2014 and the results were in good agreement with the experimental data.

In Figure 9 vertical and horizontal (middle plane) sections of the TAPIRO model produced by the MCNP plotter are represented with the indication of some main part of the nuclear reactor.

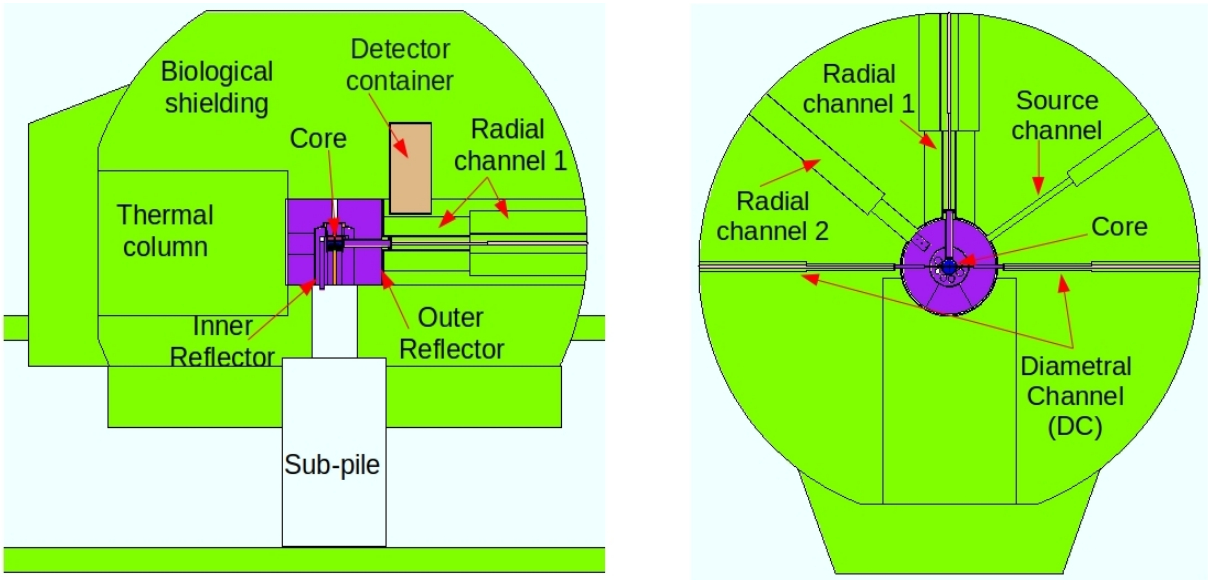

(a) (b)

Figure 9: MCNP plotter of vertical (a) and horizontal (middle plane) (b) sections of the TAPIRO model.

The MCNP input of TAPIRO model was modified by inserting void spheres of 0.5 cm in diameter centered in the average foil positions of Table 3. In Figure 10, the experimental positions are indicated on

two horizontal square sections passing through the tangential channel and the radial channel 2 axes. The neutron spectra were estimated by a “track length estimator” (tally 4 in MCNP nomenclature) of the flux in 8 spheres integrated into the energy intervals of Table 18 of Appendix A. The simulations were carried out with version 6.2 of MCNP [55] code and the ENDF/B-VIII.0 [20] neutron cross sections.

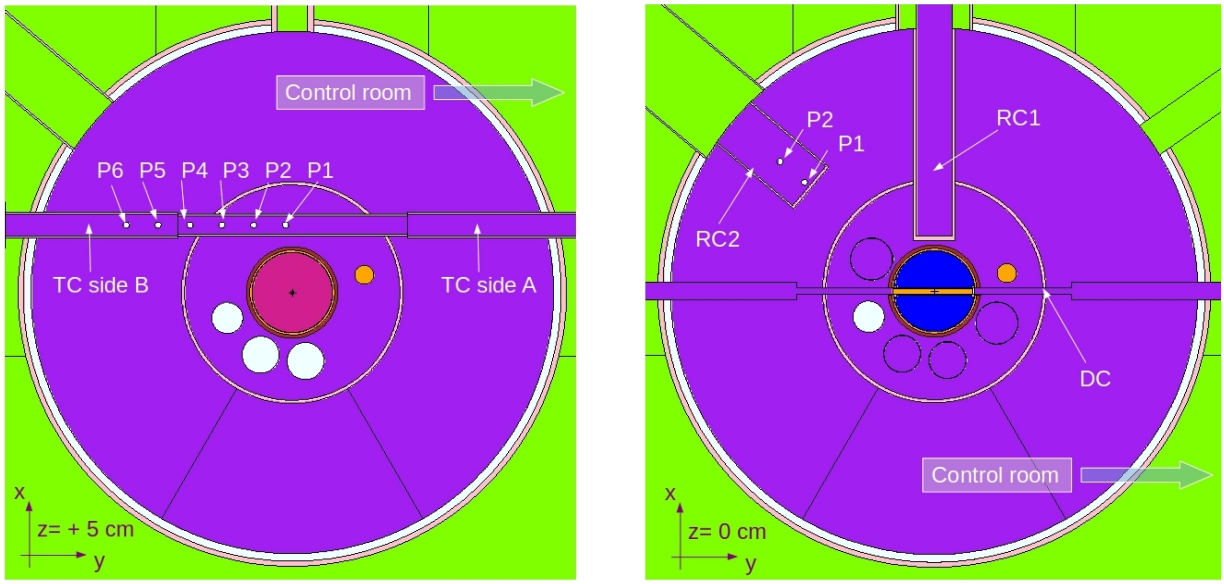

(a) (b)

Figure 10: horizontal sections of the reflector at two different horizontal heights with the indication of the experimental positions: (a) section at 5 cm from the core center with the TCB foils position; (b) core middle plane section with the RC2 foils positions.

The simulated energy differential neutron spectra in the eight positions are reported in Figure 11 where the MCNP results are represented as histograms (black lines) and superimposed with continuous interpolating spline functions (azure lines). The spectra per unit lethargy $E \cdot \varphi(E)$ in function of energy are reported in Figure 12, which gives the best visual picture of relative neutron energies and the spectra, that are depurated by the neutron slowing down. In the following, all the neutron energy spectra will be represented per unit lethargy.

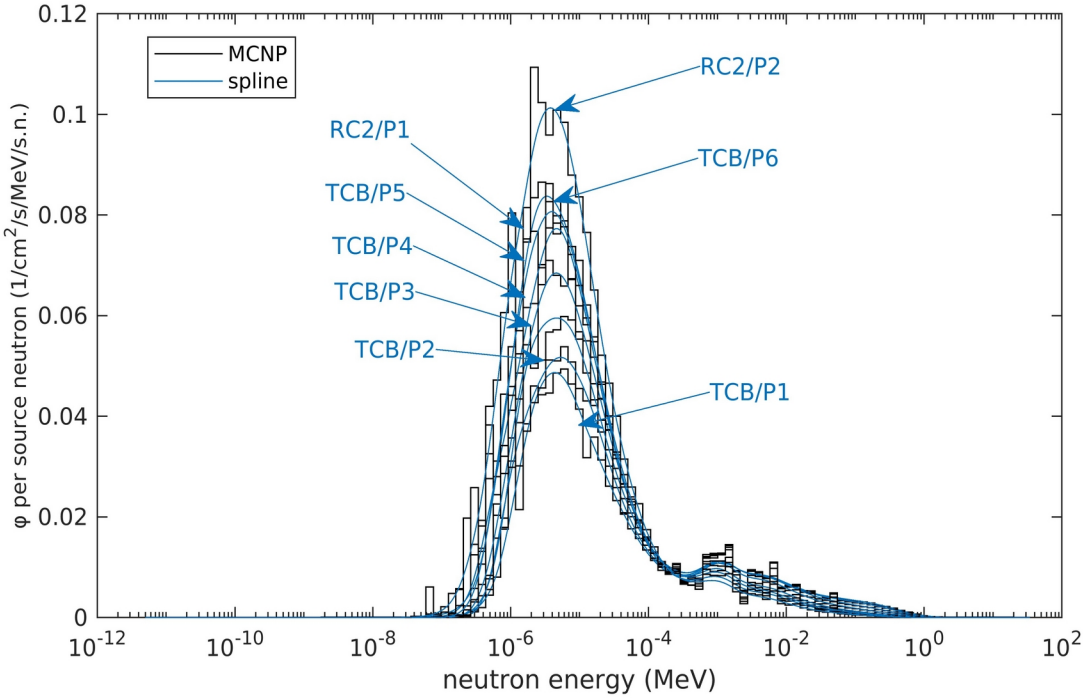

Figure 11: neutron energy differential spectra per source neutron estimated by MCNP (black line) in the eight experimental positions. In azure the curves provided by the interpolating cubic splines.

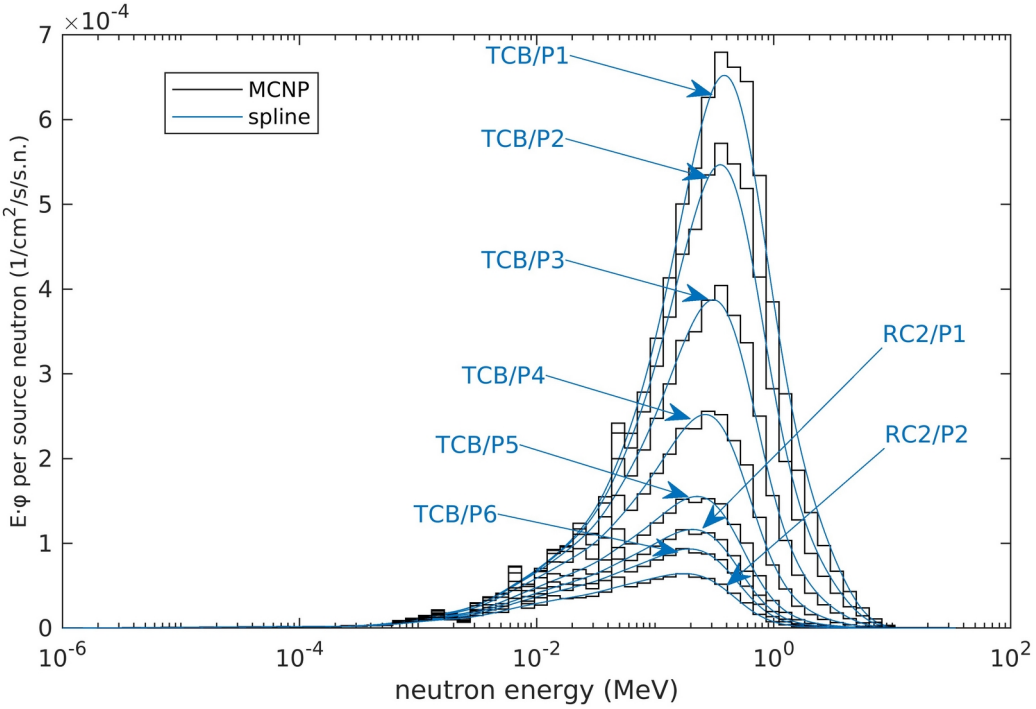

Figure 12: neutron spectra per unit lethargy and per source neutron estimated by MCNP (black line) in the eight experimental positions. In azure the curves provided by the interpolating cubic splines.

The total fluxes calculated by relation (30) with the experimental values of the saturated activities per target nucleus, the IRDFF-II cross-sections of ^{59}Co(n,γ), ^{27}Al(n,α), and ^{63}Cu(n,γ)

reactions and the *a priori* energy shapes functions g_0 obtained normalizing to 1 the spline functions of Figure 11, are reported in Table 4. In this table, for each foil position, the three total fluxes are reported along with the averaged value and the maximum deviations. The discrepancies range from a minimum of 10.51 % in the TCB/P5 position to maximum of 157.51 % for the position TCB/P6.

Table 4: total fluxes of the *a priori* neutron energy spectra

MCNP+spline: total neutron flux in n/cm²/s							
Channel	**Position I.D.**	**from ^{59}Co(n,γ) reaction** Φ_{Co}	**from ^{27}Al(n,α) reaction** Φ_{Al}	**from ^{63}Cu(n,γ) reaction** Φ_{Cu}	**Average flux** $\overline{\Phi}$	**Maximum absolute difference** $\max\lvert\Phi_i - \Phi_j\rvert$	$\frac{\max\lvert\Phi_i - \Phi_j\rvert}{\overline{\Phi}}$ **(%)**
TC/B	P1	3.41E+11	4.31E+11	3.85E+11	3.86E+11	9.01E+10	23.34
	P2	2.82E+11	1.92E+11	2.90E+11	2.55E+11	9.76E+10	38.31
	P3	1.99E+11	2.09E+11	2.02E+11	1.79E+11	6.77E+10	37.89
	P4	1.32E+11	9.25E+10	1.31E+11	1.18E+11	3.90E+10	32.92
	P5	8.14E+10	7.32E+10	7.88E+10	7.78E+10	8.18E+09	10.51
	P6	5.43E+10	6.00E+10	5.68E-15	3.81E+10	6.00E+10	157.51
RC2	P1	6.02E+10	6.91E+10	5.93E+10	6.46E+10	9.73E+09	15.06
	P2	3.23E+10	7.88E+10	3.36E+10	5.55E+10	4.65E+10	83.72

The saturated activities per target nucleus of the three reactions ^{59}Co(n,γ), ^{27}Al(n,α), and ^{63}Cu(n,γ) were calculated by means of the relation (39) with the IRDFF-II cross-sections and the average total fluxes of the *a priori* spectra reported in the sixth column of Table 4. The results of these calculated activities, referred to as *a priori* saturated activities, are reported in Tables 5, 6, and 7 and compared with the experimental values. The discrepancies between the calculated and measured values are quantified in the last columns of the three Tables 5, 6, and 7 where it should be noted that only in two cases the relative error falls below 1% and in some cases exceed 40%.

The discrepancies between the calculated and measured values of the saturated specific activities were drastically reduced by the neutron spectra with the adjustment procedure described in the previous paragraph 7.2.1 . The results of the adjustment are reported in the next paragraph.

Table 5: *a priori* saturated activity per target nucleus of the reaction $^{59}Co(n,\gamma)$

59Co(n,γ): reaction rate per target nucleus (1/s) - from MCNP+spline spectra				
Channel	**Position I.D.**	**Experiment (E)**	**Calculated (C)**	**(C/E-1)%**
TC/B	P1	2.0411E-14 (0.5%)	2.3089E-14	13.12
	P2	2.0353E-14 (0.5%)	1.8395E-14	-9.62
	P3	2.0470E-14 (0.5%)	1.8373E-14	-10.25
	P4	1.9151E-14 (0.5%)	1.7252E-14	-9.92
	P5	1.6969E-14 (0.5%)	1.6221E-14	-4.41
	P6	1.6290E-14 (0.5%)	1.6140E-14	-0.92
RC2	P1	1.5956E-14 (0.5%)	1.6669E-14	4.47
	P2	1.4452E-14 (0.5%)	2.1589E-14	49.38

Table 6: *a priori* saturated activity per target nucleus of the reaction $^{27}Al(n,\alpha)$

27Al(n,α): reaction rate per target nucleus (1/s) - from MCNP+spline spectra				
Channel	**Position I.D.**	**Experiment (E)**	**Calculated (C)**	**(C/E-1)%**
TC/B	P1	2.9733E-17 (0.5%)	2.6609E-17	-10.51
	P2	9.6969E-18 (0.5%)	1.2840E-17	32.41
	P3	4.0118E-18 (0.5%)	5.3245E-18	32.72
	P4	1.4461E-18 (0.5%)	1.8520E-18	28.07
	P5	5.9136E-19 (0.5%)	6.2848E-19	6.28
	P6	3.1740E-19 (0.6%)	2.8450E-19	-10.37
RC2	P1	3.3488E-19 (0.4%)	3.0477E-19	-8.99
	P2	1.8511E-19 (0.4%)	1.1333E-19	-38.78

Table 7: *a priori* saturated activity per target nucleus of the reaction $^{63}Cu(n,\gamma)$

63Cu(n,γ): reaction rate per target nucleus s-1 (from MCNP+spline spectra)				
Channel	**Position I.D.**	**Experiment (E)**	**Calculated (C)**	**(C/E-1)%**
TC/B	P1	1.5415E-14 (0.5%)	1.5437E-14	0.14
	P2	1.3281E-14 (0.5%)	1.1667E-14	-12.15
	P3	1.1250E-14 (0.5%)	9.9347E-15	-11.69
	P4	8.9884E-15 (0.5%)	8.1044E-15	-9.83
	P5	6.4518E-15 (0.5%)	6.3692E-15	-1.28
	P6	4.6797E-15 (0.5%)	5.3481E-15	14.28
RC2	P1	5.4730E-15 (0.5%)	5.7978E-15	5.93
	P2	3.8033E-15 (0.5%)	5.4552E-15	43.43

7.2.3 Results of the neutron spectra adjustment

The data reported in Tables 5 and 6 of the previous paragraph, related to the prior estimations of the saturated activities of the ^{59}Co(n,γ) and ^{27}Al(n,α) reactions in the eight experimental positions, were improved, in terms of differences with the corresponded experimental values, applying the neutron spectra adjustment procedure described in paragraph 7.2.1. As mentioned, only the experimental data of ^{59}Co(n,γ) and ^{27}Al(n,α) were used for the neutron spectra adjustment because the activities of the reaction ^{63}Cu(n,γ) were used for adjusting the IRDFF-II neutron radiative capture cross-section of ^{63}Cu. Following the scheme of Figure 8 of paragraph 7.2.1, the initialization of the iterative adjustment algorithm comprises the initial energy shape functions g_0, the experimental values of the saturated activities per target nucleus, the IRDFF-II evaluated cross-sections of ^{59}Co(n,γ) and ^{27}Al(n,α) reactions and the convergence tolerance ϵ. The initial energy shape functions g_0 for each experimental position were obtained normalizing to 1 the spline functions interpolating the MCNP results reported in the previous paragraph. The experimental values of the ^{59}Co(n,γ) and ^{27}Al(n,α) reaction activities were those reported for each position in the two last columns of Table 3. The evaluated cross-sections of ^{59}Co(n,γ) and ^{27}Al(n,α) reactions were downloaded from the official website [57] of the current version of the International Reactor Dosimetry and Fusion File IRDFF-II cross-sections [18]. Figure 13 reports the two neutron cross-sections ^{59}Co(n,γ) and ^{27}Al(n,α) with superimposed the percentage relative uncertainty evaluated as the ratio between the standard deviation and the mean at each neutron energy. For the convergence tolerance ϵ was chosen the value 10^{-4} that corresponds to an average relative difference between the total fluxes obtained by the two reactions of $10^{-4}/2 = 5 \cdot 10^{-5}$.

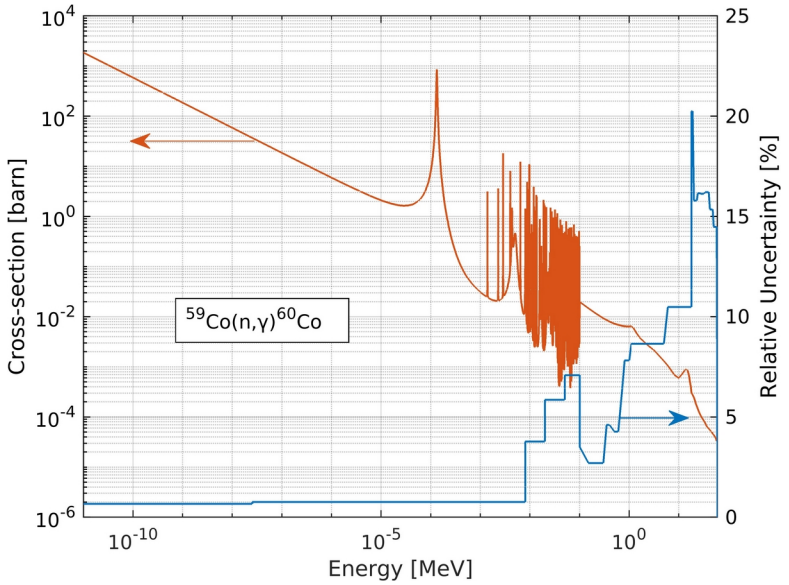

(a)

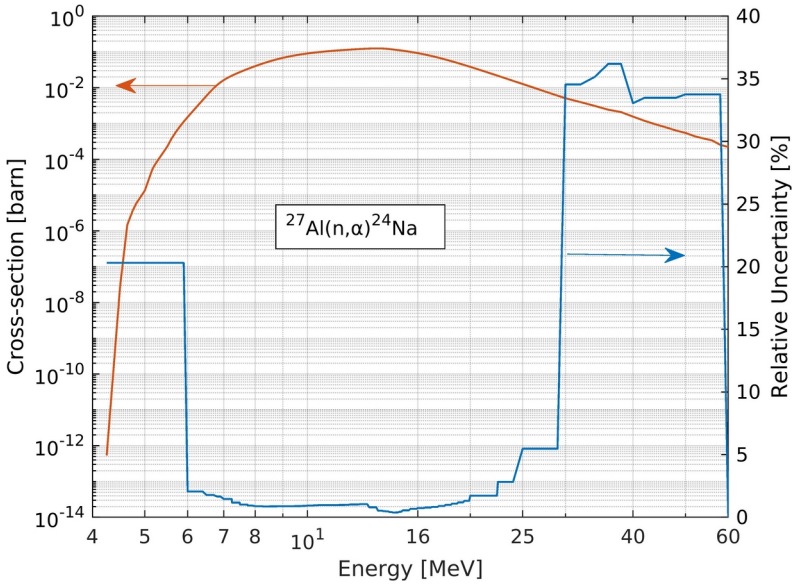

(b)

Figure 13: IRDFF-II neutron cross-sections of the reactions (a) ^{59}Co(n,γ), and (b) ^{27}Al(n,α). The percentage relative uncertainties curves are superimposed to the cross-section with the y-axis scale on the right.

The uncertainties on the experimental activities values and the evaluated cross-sections were "propagated" with the Monte Carlo technique as described in Chapter 5. Based on the resources available on the CRESCO scientific computing infrastructure, the iteration algorithm of Figure 8 of paragraph 7.2.1 was replicated 528[1] times for each case. In each replica, the probability density functions, supposed normal, of the measured activities and IRDFF-II cross-sections were sampled. The means and standard deviations were obtained from Table 3 for the activities, and from the IRDFF-II files for the evaluated cross-sections.

1 Each node of cresco6 has 48 CPUs and the utilized queue accepts the submission of jobs with a number of CPUs that must be a multiple of 48. 528 is a multiple of that number.

The final result is a set of spline curves $\{\widetilde{\varphi}_j\}_{j=1,2,\ldots,528}$ for each experimental position that forms a sample of continuous functions. For each energy E and foil position, the set of non-negative real numbers $\{\widetilde{\varphi}_j(E)\}_{j=1,2,\ldots,528}$ was treated as a sample of a probability distribution from which were calculated the basic statistical quantities: mean, standard deviation, and 95% confidence interval.

The first consequence of the minimization of the cost function defined by (35) was the reduction of the differences between the total fluxes $\widetilde{\Phi}_i$ obtained by the relation (37) for the two reactions ^{59}Co(n,γ) and ^{27}Al(n,α):

$$\widetilde{\Phi}_i = \frac{a_i^{exp}}{\int_0^\infty \sigma_i(E)\cdot\widetilde{g}(E)dE} \quad \text{with} \quad i=1,2 \tag{47}$$

The total fluxes in each position are reported in Table 8 along with the average values and the maximum differences. In brackets are reported the percent relative uncertainty resulting from the Monte Carlo propagation of uncertainties.

Table 8: total neutron fluxes of the adjusted spectra

Total neutron flux in n/cm^2/s						
Channel	**Position I.D.**	**From ^{59}Co(n,γ) reaction**	**From ^{27}Al(n,α) reaction**	**Average flux $\overline{\Phi}$**	**Maximum absolute difference $\max\lvert\Phi_{Co}-\Phi_{Al}\rvert$**	**$\frac{\max\lvert\Phi_{Co}-\Phi_{Al}\rvert}{\overline{\Phi}}$ (%)**
TC/B	P1	4.6697E+11 (5.35%)	4.6757E+11 (5.42%)	4.6727E+11 (7.62%)	5.99E+08	0.13
	P2	3.1367E+11 (4.97%)	3.1424E+11 (5.09%)	3.1395E+11 (7.12%)	5.74E+08	0.18
	P3	2.1450E+11 (4.42%)	2.1485E+11 (4.55%)	2.1467E+11 (6.34%)	3.56E+08	0.17
	P4	1.3553E+11 (3.11%)	1.3590E+11 (3.23%)	1.3571E+11 (4.48%)	3.68E+08	0.27
	P5	7.4181E+10 (2.59%)	7.3953E+10 (2.66%)	7.4067E+10 (3.71%)	2.28E+08	0.31
	P6	4.9842E+10 (3.04%)	4.7381E+10 (2.91%)	4.8611E+10 (4.22%)	2.46E+09	5.06
RC2	P1	5.7987E+10 (2.12%)	5.7967E+10 (2.25%)	5.7977E+10 (3.09%)	2.03E+07	0.04
	P2	3.9017E+10 (2.80%)	3.9097E+10 (2.87%)	3.9057E+10 (4.01%)	7.95E+07	0.20

Some considerations can be made on the data of Table 8, the first is that comparing the maximum relative deviations reported in the last column with the analogous values reported in Table 4 for the *a priori* neutron spectra, the dispersion of the values of the total fluxes is significantly reduced. All the differences are below 1% except for the position P6 of the tangential channel where the relative deviation is about 5.1%. On the contrary, the values of Table 4 for the *a priori* neutron spectra are greater than 10% reaching the maximum of 157.51% for the TCB/P6 position.

A further consideration is on the percent errors of total fluxes that show a decreasing trend increasing the distance from the core center, although the experimental relative errors are substantially constant. The justification of this behavior is in the softening of the neutron spectra moving away from the core center and in the reduction of the uncertainties of the ^{59}Co(n,γ) cross-sections reducing the neutron energy as shown in Figure 13a. The uncertainties of the ^{27}Al(n,α) cross-section are irrelevant because this reaction affects only the high-energy and low-intensity portion of the neutron spectra. The softening of the neutron spectra is proved by the reduction of the spectrum averaged neutron energy reported in Table 9.

Table 9: neutron energies averaged on the adjusted neutron spectra

$\overline{E} = \int_0^\infty E \cdot \widetilde{g}(E) dE$ **spectrum averaged neutron energy (MeV)**					
Channel	**Position I.D.**	**Average distance from the core (cm)**	**Mean**	**Standard deviation**	**Relative error (%)**
TCB	P1	11.755	0.585	0.034	5.9
	P2	13.127	0.472	0.026	5.5
	P3	16.017	0.393	0.022	5.5
	P4	19.762	0.287	0.011	4.0
	P5	23.971	0.2042	0.0078	3.8
	P6	28.440	0.1609	0.0076	4.7
RC2	P1	26.357	0.1949	0.0062	3.2
	P2	31.357	0.1995	0.0089	4.5

The average total fluxes in the function of the distance from the core center are shown in Figure 14 and compared with the values obtained with the *a priori* neutron spectra. The adjusted fluxes are, in almost all positions, greater than the *a priori* fluxes except for the positions TCB/P5, RC2/P1, and RC2/P2 where, however, the values are very close.

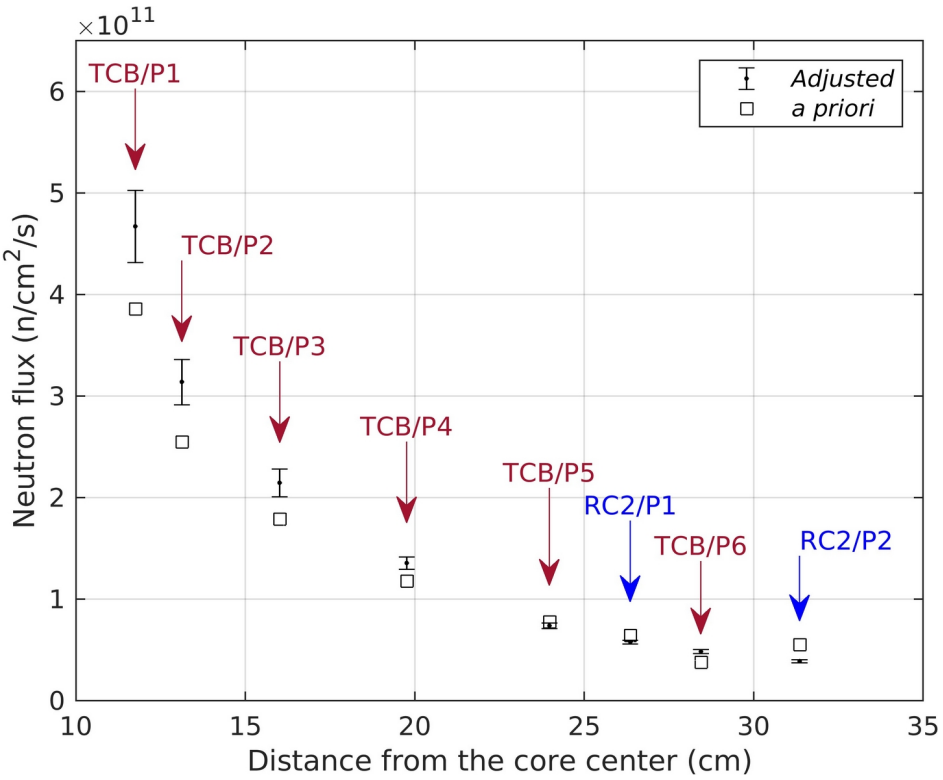

Figure 14: radial profile of the total neutron flux for both adjusted and *a priori* neutron energy spectra.

The adjusted neutron energy spectra per unit lethargy are shown in Figure 16 for the six positions of the tangential channel and in Figure 17 for the two positions of radial channel 2. The 95% confidence region is represented as a gray zone around the average value represented by the continuous black line. The percent relative uncertainty, calculated as the ratio between the estimation of the standard deviation and mean of the distributions at each energy, is superimposed to the corresponding neutron spectra plot as a green line with the y-axis scale on the right. For comparison, the initial neutron energy spectra per unit lethargy is reported as a red line.

The percent relative uncertainties are below 15% for neuron energy not exceeding 10 MeV for all the positions and have a decreasing trend moving away from the core center. Similarly to the total fluxes, this behavior is justified by the softening of the neutron spectra and, as reported in the subsequent uncertainty analysis, the predominance of the cross-section contribution to the total uncertainties.

The comparison between the *a priori* and the adjusted neutron energy spectra reveals that the adjusted neutron spectra are above the corresponding *a priori* spectra except for the positions TCB/P5, TCB/P6, and RC2/P1 partially confirming the consideration made for the total fluxes.

The application of the proposed cross-section adjustment method requires the utilization of different neutron energy spectra. The differences must be mainly in the energy shape function g rather than in the total flux. Figure 15 reports the differences, in unit lethargy, of the energy shape functions g with respect to the shape function of the neutron spectrum in TCB/P1 position that is, among the examined positions, the position where the spectrum is the most energetic. Two regions can be identified in Figure 15, one above the neutron energy of 0.29 MeV, where the differences are negatives, and one below 0.29 MeV where the curves are positives. In the first region, the neutron energy spectrum in TCB/P1 is, as expected, more energetic than the others. Below 0.29 MeV the other neutron energy spectra prevail on the TCB/P1 energy shape for their less energetic components. The neutron energy shape function in TCB/P5, TCB/P6, RC2/P1, and RC2/P2 show only little differences, in future work more attention must be paid to the choice of the experimental positions to consider the largest possible variety of neutron energy spectra.

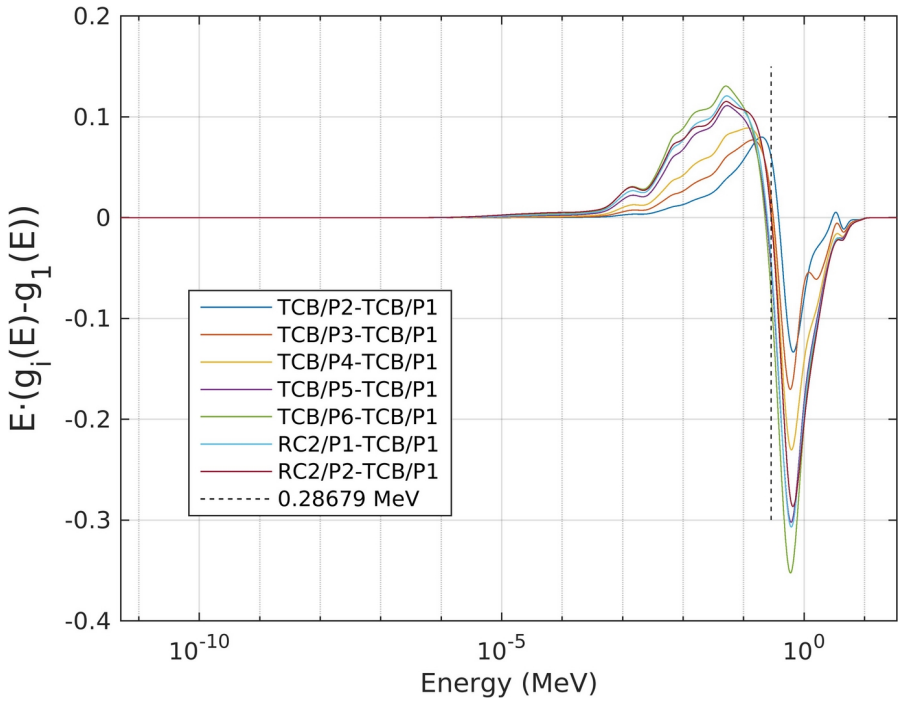

Figure 15: differences in unit lethargy between the energy shape functions respect to the TCB/P1 position.

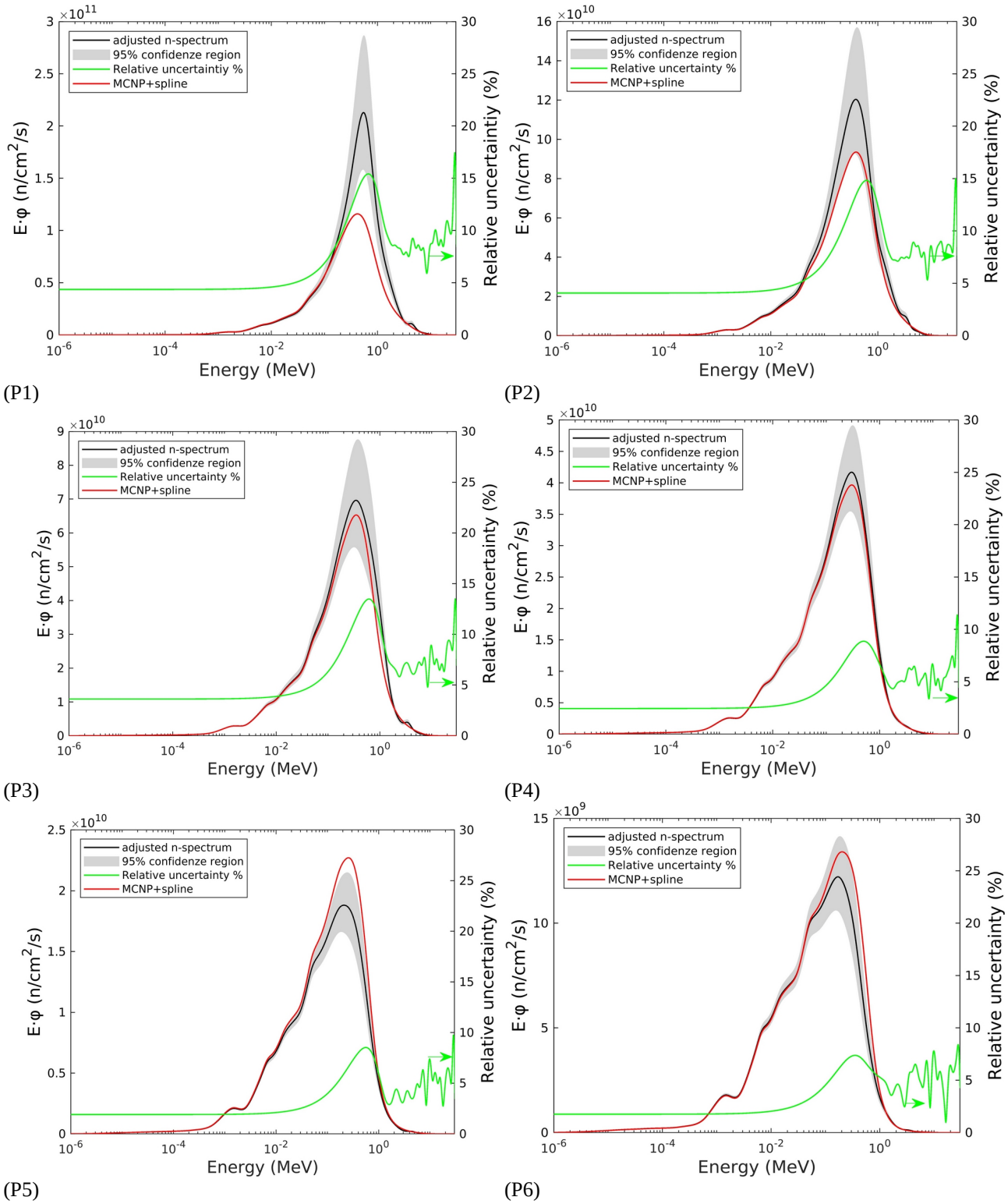

Figure 16: neutron energy spectra per unit lethargy with the 95% confidence prediction regions in the six positions (from P1 to P6) of side B of the tangential channel after the adjustment. The initial *a priori* spectra (the MCNP+spline curves) and the percentage relative uncertainty curves are superimposed.

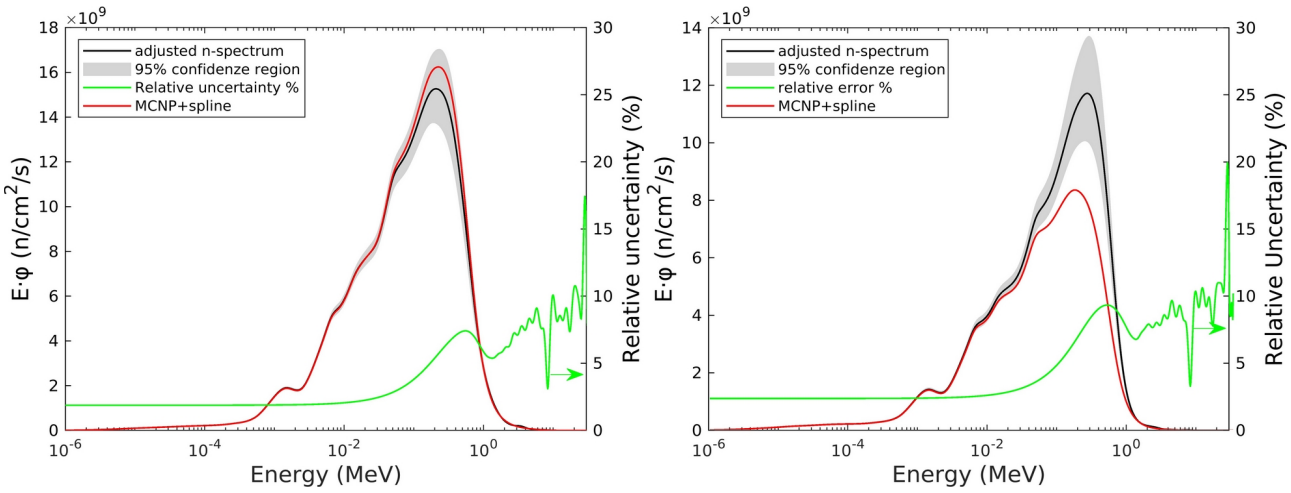

Figure 17: neutron energy spectra per unit lethargy with the 95% confidence prediction regions in the two positions P1 and P2 of radial channel 2. The initial *a priori* spectra (the MCNP+spline curves) and the percentage relative uncertainty curves are superimposed.

The best estimation of the saturated activities per target nucleus of the ^{59}Co(n,γ) and ^{27}Al(n,α) reactions, calculated with the relation (39), are reported in Tables 10 and 11 and compared with the *a priori* and experimental values. The calculated values are in excellent agreement with the experimental values except for the activities calculated in the position TCB/P6, where the relative uncertainty remains above 1% but below 3%. The calculated relative uncertainties on the saturated activities are higher for the ^{27}Al(n,α) reactions but anyway below 0.6%. The calculated and experimental activities are also reported on comparison graphs in Figures 18 and 19 along with the linear fit, the 95% confidence region, and the equal values line (bisector). In Figure 19 both axes are in logarithmic scale because the activity values for the ^{27}Al(n,α) reactions ranges by 2 order of magnitude, from 1E-19 to 1E-17.

Table 10: best estimation of the ^{59}Co(n,γ) saturate activities per target nucleus and comparison with the experimental values

^{59}Co(n,γ): reaction rate per target nucleus (1/s/nucleus)						
Channel	**Position I.D.**	**Experiment (E)**	**MCNP+spline**	**(C/E-1)%**	**Adjusted**	**(C/E-1)%**
TC/B	P1	2.0411E-14 (0.5%)	2.31055E-14	13.2	2.04229E-14 (0.53)	0.0585
	P2	2.0353E-14 (0.5%)	1.71228E-14	-15.9	2.03721E-14 (0.55)	0.0941
	P3	2.0470E-14 (0.5%)	1.71566E-14	-16.2	2.04820E-14 (0.53)	0.0588
	P4	1.9151E-14 (0.5%)	1.63109E-14	-14.8	1.91814E-14 (0.54)	0.1589
	P5	1.6969E-14 (0.5%)	1.61162E-14	-5.0	1.69424E-14 (0.51)	-0.1567
	P6	1.6290E-14 (0.5%)	1.71480E-14	5.3	1.58868E-14 (0.52)	-2.4753
RC2	P1	1.5956E-14 (0.5%)	1.71357E-14	7.4	1.59556E-14 (0.49)	-0.0026
	P2	1.4452E-14 (0.5%)	2.48574E-14	72.0	1.44738E-14 (0.50)	0.1506

Table 11: best estimation of the $^{27}Al(n,\alpha)$ saturate activities per target nucleus and comparison with the experimental values

$^{27}Al(n,\alpha)$: reaction rate per target nucleus (1/s/nucleus)						
Channel	**Position I.D.**	**Experiment (E)**	**MCNP+spline**	**(C/E-1)%**	**Adjusted**	**(C/E-1)%**
TC/B	P1	2.9733E-17 (0.5%)	2.66278E-17	-10.4	2.97156E-17 (0.58%)	-0.0584
	P2	9.6969E-18 (0.5%)	1.19516E-17	23.3	9.68822E-18 (0.59%)	-0.0895
	P3	4.0118E-18 (0.5%)	4.97205E-18	23.9	4.00800E-18 (0.47%)	-0.0946
	P4	1.4461E-18 (0.5%)	1.75098E-18	21.1	1.44433E-18 (0.55%)	-0.1225
	P5	5.9136E-19 (0.5%)	6.24400E-19	5.6	5.92247E-19 (0.56%)	0.1500
	P6	3.1740E-19 (0.6%)	3.02276E-19	-4.8	3.25626E-19 (0.58%)	2.5917
RC2	P1	3.3488E-19 (0.4%)	3.13311E-19	-6.4	3.34958E-19 (0.46%)	0.0234
	P2	1.8511E-19 (0.4%)	1.30487E-19	-29.5	1.84974E-19 (0.44%)	-0.0737

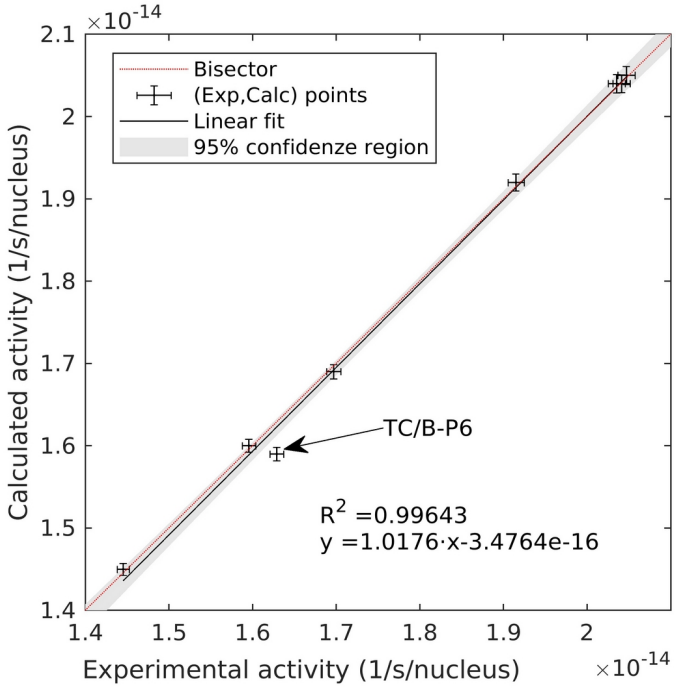

Figure 18: experimental vs. calculated values of the $^{59}Co(n,\gamma)$ saturate activities.

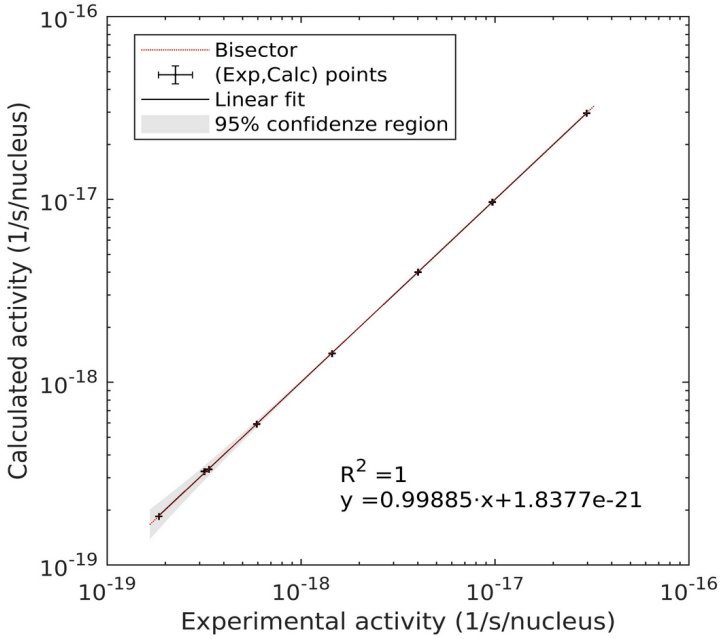

Figure 19: experimental vs. calculated values of the ^{27}Al(n,α) saturate activities.

The application of the propagation of distributions technique for the uncertainties evaluations was performed considering the experimental uncertainties on the measured activities and the evaluated IRDFF-II cross-sections. As mentioned in Chapter 5, a third source of uncertainty may be identified in the stochastic hill-climbing algorithm for its intrinsic stochastic nature. This contribution should be subtracted from the final results because it does not have a physical origin, and, in general, assumes values negligible with respect to the other uncertainties contributions. The analysis of the contributions to the total activities of the two ^{59}Co(n,γ) and ^{27}Al(n,α) reactions was made by performing, for each reaction and experiential position, three separate optimizations and propagation of uncertainties with:

a) only the experimental activities uncertainties;

b) only the IRDFF-II cross-sections uncertainties;

c) neither of those two.

The first two cases contain also the intrinsic components due to the optimization algorithm, whereas the third case contains only the stochastic component. Tables 12 and 13 report the relative uncertainties for the ^{59}Co(n,γ) and ^{27}Al(n,α) activities calculated for the three aforementioned cases and each experimental position. The intrinsic stochastic component, reported in the fifth column of

Tables 12 and 13, is indicated with MC (Monte Carlo) and can be neglected when compared with the other two uncertainty sources. But, again, the results for the TCB/P6 position have the highest relative uncertainties, at least 4 times higher than the one in the other positions, and become comparable with the relative uncertainties evaluated in the other two optimization cases. The subtraction of the MC component to the total values is practically irrelevant, or nearly, irrelevant for all cases. The comparison of the values of the last columns of Tables 12 and 13 with the corresponding relative uncertainty values reported in brackets into the sixth columns of Tables 10 and 11 indicates that only for the TCB/P6 position there is a slight difference.

Comparing the percent errors of each position it is evident that the experimental uncertainty of the activities constitutes the predominant contribution into the composition of the total activities percent error. The comparison between the three components is also shown, even if only for the position TCB/P1, in Figure 20a and 20b where the three components are reported as histograms. In those Figures is clearly shown the predominance of the contribution of the activities uncertainties and the negligibly of the cross-section and MC components.

Table 12: relative uncertainty components for the $^{59}Co(n,\gamma)$ reaction rate

Channel	Position I.D.	Activities+MC	Cross-section+MC	MC	Total - MC
TCB	P1	0.52%	0.25%	0.0130%	0.53%
	P2	0.50%	0.27%	0.0104%	0.55%
	P3	0.50%	0.23%	0.0098%	0.53%
	P4	0.48%	0.27%	0.0102%	0.54%
	P5	0.44%	0.22%	0.0379%	0.51%
	P6	0.43%	0.32%	0.1517%	0.49%
RC2	P1	0.47%	0.16%	0.0213%	0.49%
	P2	0.47%	0.15%	0.0107%	0.50%

Table 13: relative uncertainty components for the $^{27}Al(n,\alpha)$ reaction rate

Channel	Position I.D.	Activities+MC	Cross-section+MC	MC	Total - MC
TCB	P1	0.51%	0.25%	0.0130%	0.58%
	P2	0.49%	0.26%	0.0104%	0.59%
	P3	0.39%	0.23%	0.0098%	0.47%
	P4	0.51%	0.27%	0.0101%	0.55%
	P5	0.53%	0.22%	0.0380%	0.56%
	P6	0.54%	0.34%	0.1599%	0.56%
RC2	P1	0.41%	0.16%	0.0213%	0.45%
	P2	0.43%	0.15%	0.0107%	0.44%

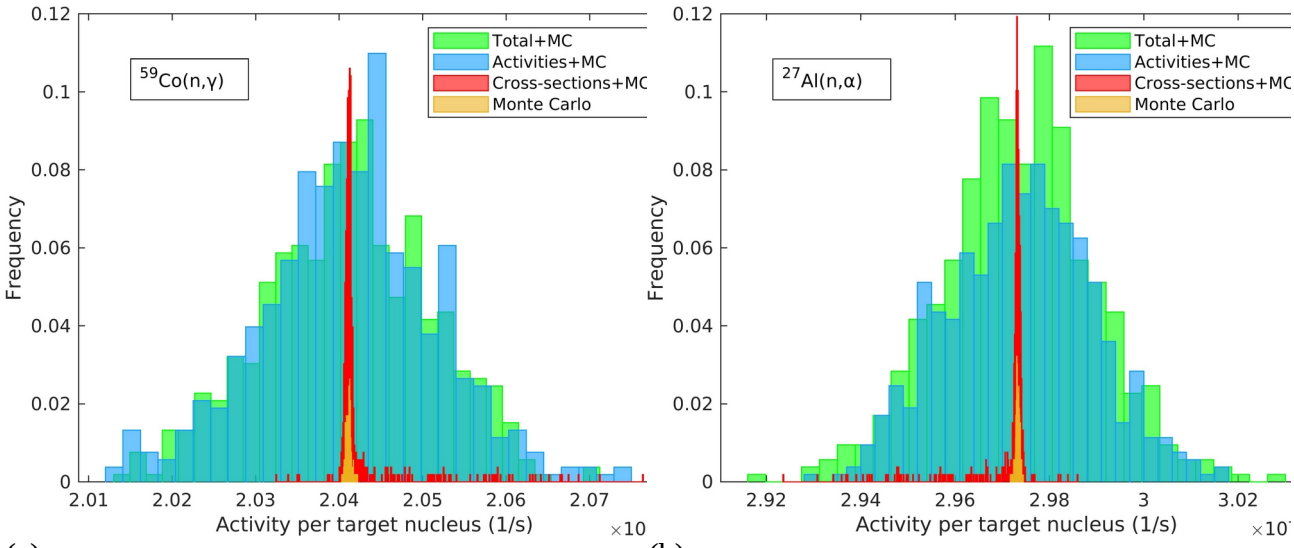

(a) (b)

Figure 20: contributions to the distribution propagation for the ^{59}Co(n,γ), on the left, and the ^{27}Al(n,α), on the right, specific saturated activity in TCB/P1 positions.

The energy dependence of the three relative uncertainties components of the neutron energy spectrum in the position TCB/P1 is shown in Figure 21. The cross-section components, the red line in the Figure, are very close to the total relative uncertainty and constitute the predominant component with a maximum of about 0.68 MeV. The total relative uncertainty, the black line in Figure 21, is obtained by subtracting the "MC" uncertainty from the "Total+MC": $\sigma_{Tot} = \sqrt{\sigma^2_{Tot+MC} - \sigma^2_{MC}}$; the same curve is reported in Figure 16P1.

The results of the uncertainty analysis for the other experimental positions lead to the same conclusions obtained for the TCB/P1 position and, for this reason, are not reported in this work.

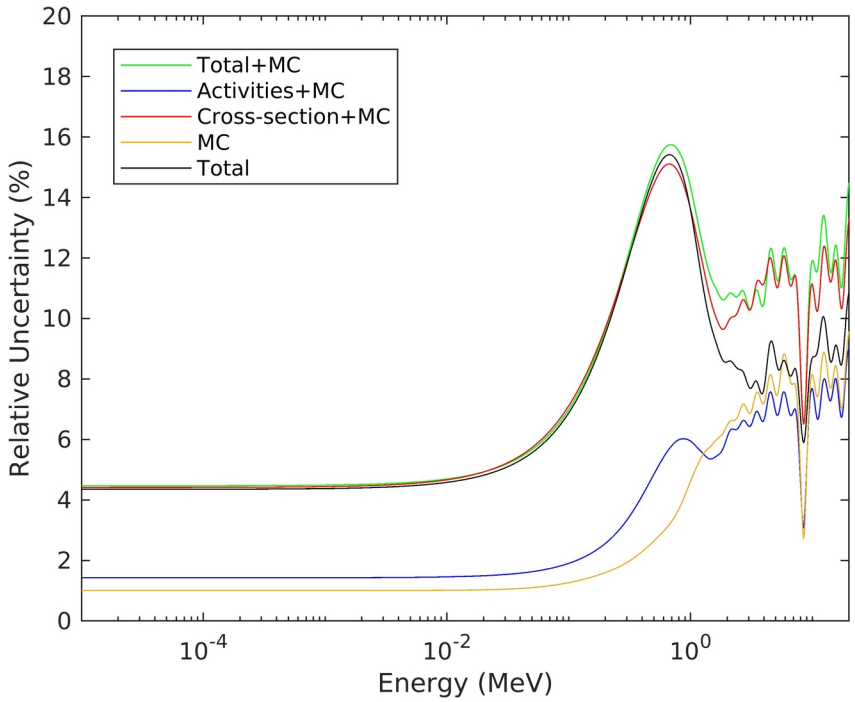

Figure 21: energy dependence of the components of the relative uncertainty for the neutron energy spectrum in the position TCB/P1

7.3. The ^{63}Cu(n,γ) cross-section adjustment

The application of the cross-section adjustment procedure was carried out considering only seven experimental positions of Table 3; the position P6 of the tangential channel was rejected because of the high difference, if compared with the results in the other positions, against the measured value. The calculated vs. experimental relative error of the ^{59}Co(n,γ) and ^{27}Al(n,α) activities in the TCB/P6 are at least 15 times higher than the values in the other positions, as observable by the last columns of Tables 10 and 11. The origin of this discrepancy should probably be sought in some error in the measured activities of the foil positioned in TCB/P6 or in the *a priori* neutron energy spectrum and then in some inaccuracy in the geometry and/or materials composition of the MCNP model of TAPIRO in proximity of that position. A possible experimental cause of this discrepancy is arduous to determine because the measurements were performed several years ago by people who are no longer available, for this reason, the only possible investigation is on the lack of correspondence between the MCNP model and the reality. This additional analysis was not performed in this work and could be included in future work. Consequently, excluding the position TCB/P6, the data utilized for the cross-section adjustment were the saturated activities per target nucleus of the ^{63}Cu(n,γ) reaction reported in the fifth column of Table 2 of paragraph 7.1, and the neutron spectra showed in Figure 16 and 17. The *a priori* information is constituted by the energy dependence of the ^{63}Cu(n,γ) cross-section of the IRDFF-II nuclear data library updated on December 9, 2020, and available on the IAEA website [18]. Figure 22 shows the neutron incident energy dependence of the cross-section and the relative uncertainty on the right y-axis scale. The energy in the IRDFF-II ^{63}Cu(n,γ) cross-section file ranges from 10 μeV to 60 MeV. It should be noted that the current IRDFF-II library was updated in 2020 for only some reactions, whereas the cross-section data of the ^{63}Cu(n,γ)^{64}Cu reaction refer to the old IRDF-2002 file for the energies between thermal to 20 MeV and the TENDL-2011 library [58] for energies from 20 MeV to 60 MeV as reported in Table 1 of [18].

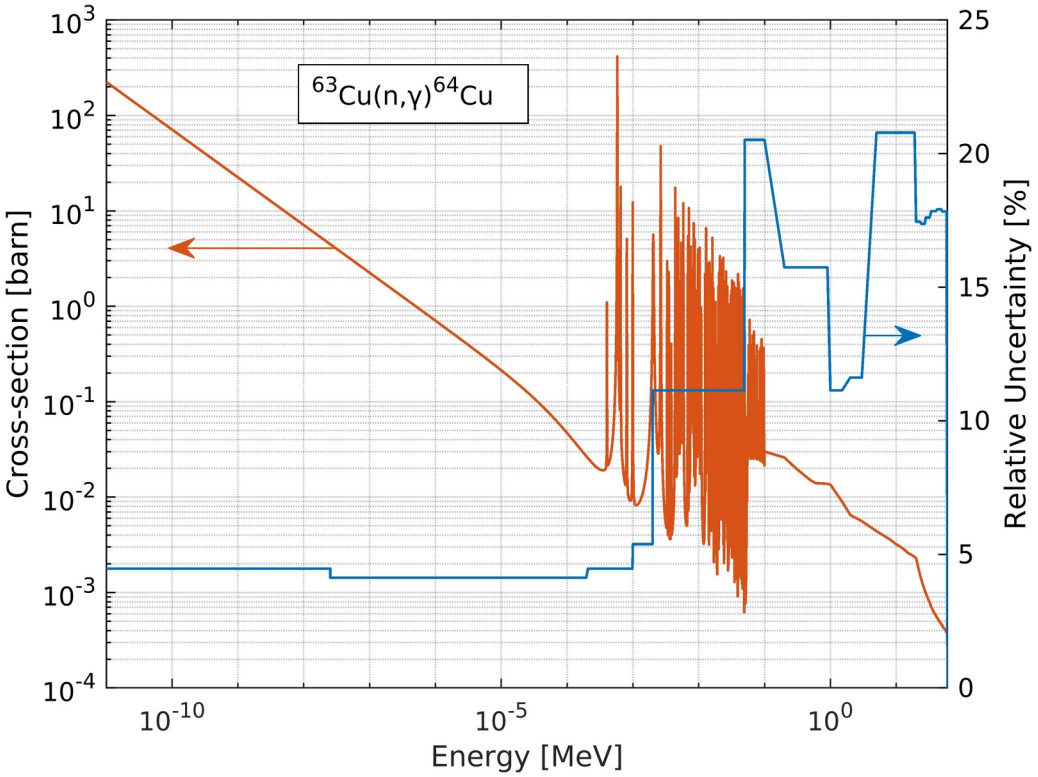

Figure 22: IRDFF-II ^{63}Cu(n,γ)^{64}Cu reaction cross-section as a function of neutron energy and relative uncertainty (y-axis scale on the right)

The first consequence of the application of the procedure reported in Chapter 4 for the cross-section adjustment is the reduction of the differences between the calculated and experimental values of the saturated activities per target nucleus of the ^{63}Cu(n,γ) reaction. In fact, the cost function is the sum of squares of the relative differences between those values, and its minimization reduces these differences. Table 14 reports the saturated activities per target nucleus calculated before (fourth column) and after (sixth column) the adjustment of the cross-section compared with the measured values, which, for convenience, were repeated in the same table. The reduction of the "distance" between the calculation and the experiment is evident. Before the adjustment, all the calculated activities overestimated the experiment by, on average, 3.5% and with a minimum of 2.17%. After the adjustment the average of the absolute relative difference is 0.36% with a maximum of 0.64%; one order of magnitude lower than before the adjustment. This situation is also graphically seen in Figure 23, where the excellent agreement between the calculated and measured values is indicated by the R-squared value, practically equal to 1, and the slope and intercept values of the best-fit linear equation, very close to the bisector.

Table 14: ^{63}Cu(n,γ) saturated activities per target nucleus before and after the cross-section adjustment

^{63}Cu(n,γ): reaction rate per target nucleus (1/s/nucleus)						
Channel	**Position I.D.**	**Experiment (E)**	**Before the adjustment**		**After the adjustment**	
			Calculated (C)	**(C/E-1)%**	**Calculated (C)**	**(C/E-1)%**
TCB	P1	1.5415E-14 (0.5%)	1.5846E-14	2.79	1.5345E-14 (1.48%)	-0.46
	P2	1.3281E-14 (0.5%)	1.3725E-14	3.34	1.3360E-14 (1.37%)	0.59
	P3	1.1250E-14 (0.5%)	1.1593E-14	3.05	1.1243E-14 (1.32%)	-0.059
	P4	8.9884E-15 (0.5%)	9.2818E-15	3.26	8.9304E-15 (1.13%)	**-0.64**
	P5	6.4518E-15 (0.5%)	6.8367E-15	5.97	6.4795E-15 (1.14%)	0.43
RC2	P1	5.4730E-15 (0.5%)	5.6746E-15	3.68	5.4719E-15 (1.15%)	-0.019
	P2	3.8033E-15 (0.5%)	3.8858E-15	**2.17**	3.8153E-15 (1.14%)	0.32

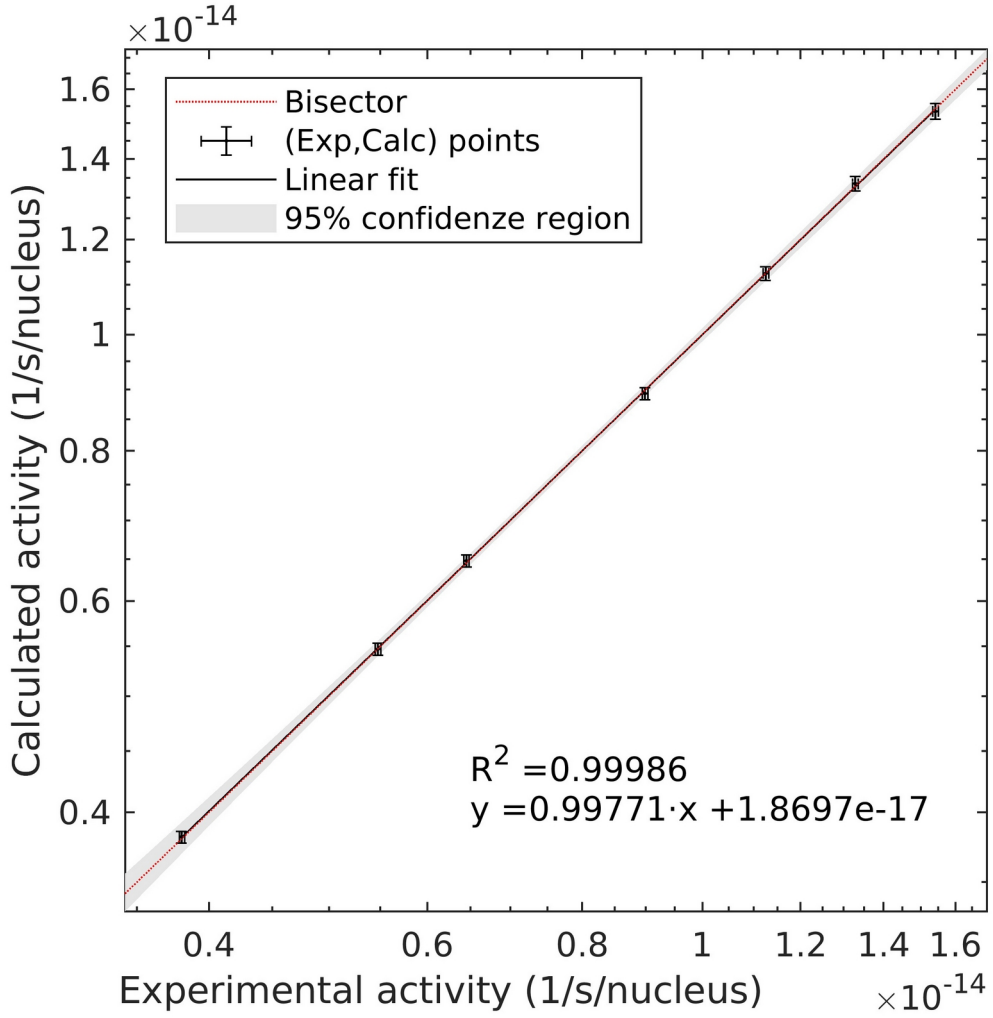

Figure 23: experimental vs. calculated values of the ^{63}Cu(n,γ) saturate activities.

The new cross-section is the main result of the adjustment procedure. The comparison between the calculated and experimental values of Table 14 is an indication of the reliability of the new cross-section, but other factors were taken into consideration for the new cross-section assessment. The deviation of the adjustment result from the evaluated *a priori* cross-section is, for example, an important factor to take into account. The evaluated cross-sections are the result of an accurate and meticulous process where the validated experimental data, obtained by different experiments performed in different laboratories with different techniques, are interpolated with the use of nuclear models. Figure 24 reports the two cross-sections, the adjusted and the *a priori* IRDFF-II energy-depended curves, with the corresponding 95% confidence regions and the three typical regions for the non-threshold neutron induce reaction: the $1/v$ region from thermal to 100 eV of neutron energy; the Resolved Resonance Region (RRR) that extended from 100 eV to 0.1 MeV and the Unresolved Resonance Region (URR) above the 0.1 MeV. The URR region was limited to the maximum neutron energy of 35 MeV in the calculations that involve the neutron energy spectra; 35 MeV is the maximum energy considered in the energy intervals in Appendix A without considering the limit in the MCNP results. The most intense peak of the Resolved Resonance Region of the ^{63}Cu(n,γ) ^{64}Cu reaction, is at 579 eV where the cross-section assumes the value of 415.8 barn.

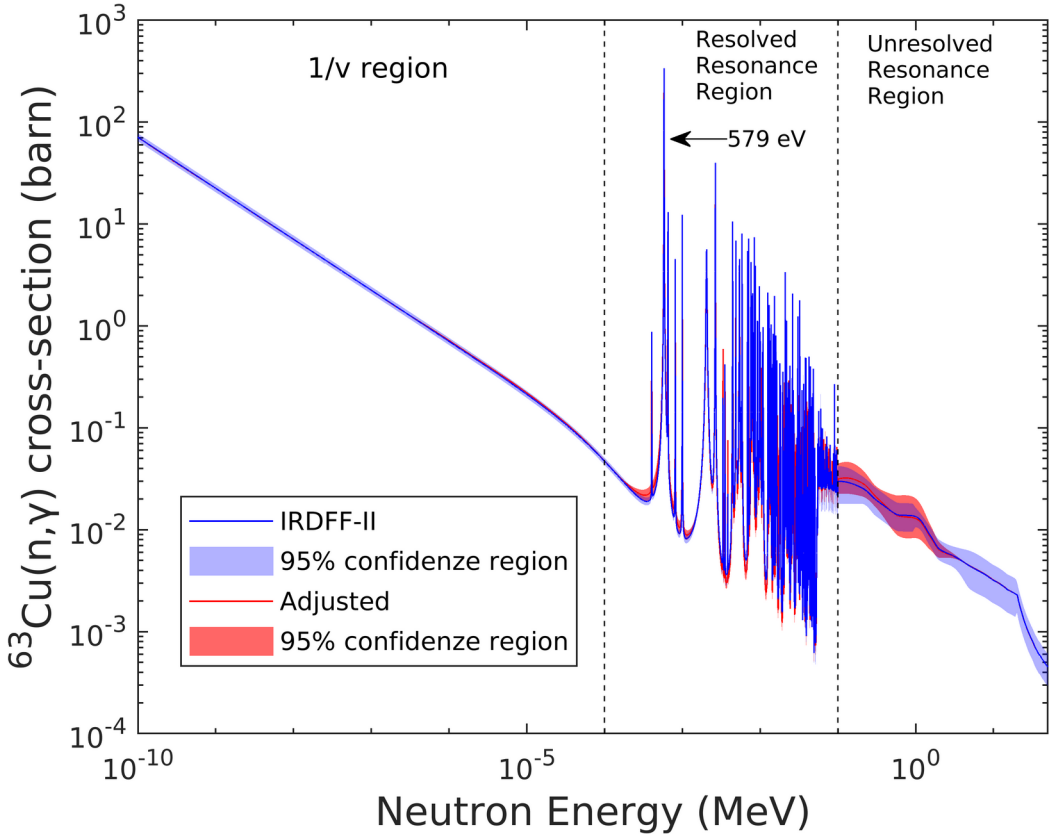

Figure 24: IRDFF-II and adjusted energy dependence of the ^{63}Cu(n,γ) ^{64}Cu reaction cross-section with the corresponding 95% confidence region

The two cross-section curves of Figure 24 differ mainly in the resonance regions whereas are practically the same in the $1/v$ region. These differences were quantified by calculating the fractions of the total saturated activity of the ^{63}Cu(n,γ) reaction in the three energy regions by using the two cross-sections and the neutron energy spectrum in each experimental position:

$$\frac{\int_{\text{Energy Region}} \sigma(E)\widetilde{\varphi}_i(E)dE}{\int_0^{\infty} \sigma(E)\widetilde{\varphi}_i(E)dE} \quad \text{with:} \begin{cases} i = 1, 2, ..., 7 \\ \text{and} \\ \sigma \text{ the adjusted of IRDFF-II cross-section} \end{cases} \tag{48}$$

The results, reported in Table 15, clearly indicate that both cross-sections provide comparable values and trends in the three energy regions. In detail:

- the contribution of the $1/v$ region is of a few percentage whereas the contribution of the resolved resonance region predominates and only in the position TCB/P1 the two resonance regions RRR and URR provide comparable values;
- the contribution to the total activity due to the $1/v$ and unresolved resonance regions gradually increases as the distance from the TAPIRO core center increases at the expense of the contribution of the unresolved region that decreases. The softening of the neutron energy spectra increasing the distance from the core center is the origin of this behavior;
- in the $1/v$ and unresolved resonance regions, the factions calculated with the IRDFF-II cross-section are systematically lower than the ones obtained with the adjusted cross-section, on the contrary, in the resolved resonance region are greater. Although the differences are minimal, a possible consideration that can be made is that, without considering the $1/v$ region, the cross-section adjusted procedure has resulted in an average increment of the cross-section in the unresolved region and a reduction in the resolved resonance region.

Table 15: relative fraction of the total saturated activities of the ^{63}Cu(n,γ) reaction calculated in the three regions ($1/v$, RRR and URR) with the adjusted and IRDFF-II cross-sections

Channel	**Position I.D.**	**Adjusted | IRDFF-II total activity fraction (%)**		
		$1/v$ region	**Resolved Resonance Region**	**Unresolved Resonance Region**
		10 μeV – 100 eV	**100 eV – 0.1 MeV**	**0.1 MeV – 34 MeV**
TCB	P1	0.35 | 0.33	53.87 | 59.03	45.78 | 40.64
	P2	0.45 | 0.43	62.38 | 67.79	37.17 | 31.78
	P3	0.61 | 0.57	70.96 | 75.71	28.43 | 23.72

	P4	0.81 | 0.75	77.21 | 81.11	21.98 | 18.14
	P5	1.10 | 1.02	82.90 | 85.94	16.00 | 13.04
RC2	P1	1.36 | 1.26	85.58 | 77.13	13.06 | 10.61
	P2	2.17 | 2.04	85.56 | 87.89	12.28 | 10.07

The origin of these "averaged" differences, resides in the energy-dependent correction function $e^{\gamma} = \widetilde{\sigma}/\sigma_0$ generated by the cross-section adjustment algorithm. This function provides a punctual relative difference between the adjusted and *a priori* cross-sections and presents a certain variability. In Figure 25 the average final correction function for the ^{63}Cu(n,γ) cross-section reaction is shown along with the limits of the three energy regions.

In the $1/v$ region, the correction is low (compared with the values in the other regions) and doesn't exceed 4%. This region gives a small and negligible contribution to the calculated total activities reported in Table 14, because the neutron flux at these energies assumes a very low value, as shown in neutron energy differential spectra of Figures 16 and 17.

In the resolved resonance region the correction function has two different trends. From 100 eV to 1.5 keV, e^{γ} is greater than 1, which means that $\widetilde{\sigma} > \sigma_0$, reaches the maximum difference at 561 eV where the adjusted cross-section is about 24% higher than the *a priori* function. At 1.5 keV the two functions are equal $\widetilde{\sigma} = \sigma_0$ and the trend is inverted at higher energy up to the upper limit of this region with a maximum difference at 9.4 keV where the adjusted cross-section is about 30% lower than that *a priori*. In this second portion of the RRR region, where the adjusted cross-section is lower than the IRDFF-II one, the neutron spectra are not negligible and higher than for lower energies.

Lastly, in the unresolved resonance region, the correction function curve has a maximum at 0.2 MeV where the adjusted cross-section is about 26% higher than the original IRDFF-II cross-section.

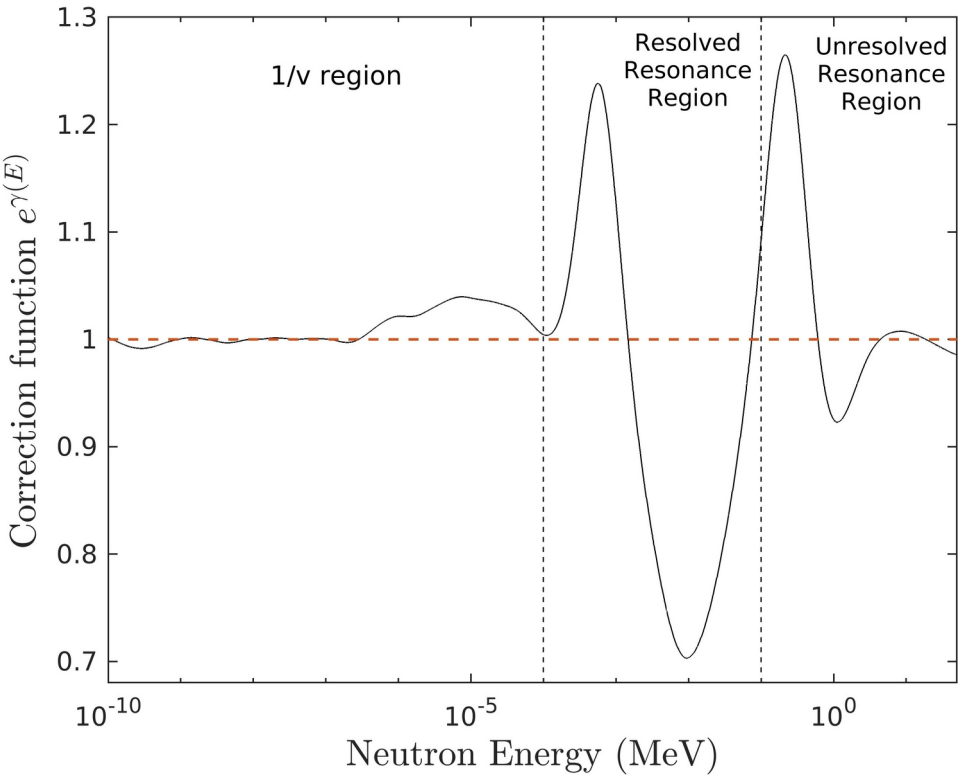

Figure 25: energy dependence of the correction function $e^{\gamma} = \widetilde{\sigma}/\sigma_0$

The IRDFF-II and the adjusted cross-section are compared in Figure 26 with the available experimental data in the unresolved resonance region [59 - 60], and [61], indicated in the Figure as Toi66, Zai68, Dik70, Man04, Kim07, and Wei17 respectively. The discrepancies between the two cross-sections, adjusted and *a priori*, are evident in Figure 26, where the adjusted cross-section is indicated by the red line and the IRDFF-II curve by the blue line. The 95% confidence regions of the two cross-sections appear to be widely superimposed and with the same order of magnitude, indicating that the adjustment process hasn't furnished an improvement in the uncertainty reduction. However, the adjusted ^{63}Cu(n,γ)^{64}Cu energy cross-section is close to data furnished by the recent time-of-flight experiment performed in 2017 and reported in [61]. This experiment, performed at flight path 14 at the Manuel Lujan Jr. Neutron Scattering Center at the Los Alamos Neutron Science Center (LANSCE), has provided 398 points, from 74 eV up to 0.69 MeV, for the ^{63}Cu(n,γ)^{64}Cu energy depended on cross-section. The orange points in Figure 26 represent only a small number of these data, the complete set of data is reported in Figure 27 along with the evaluated and adjusted cross-sections.

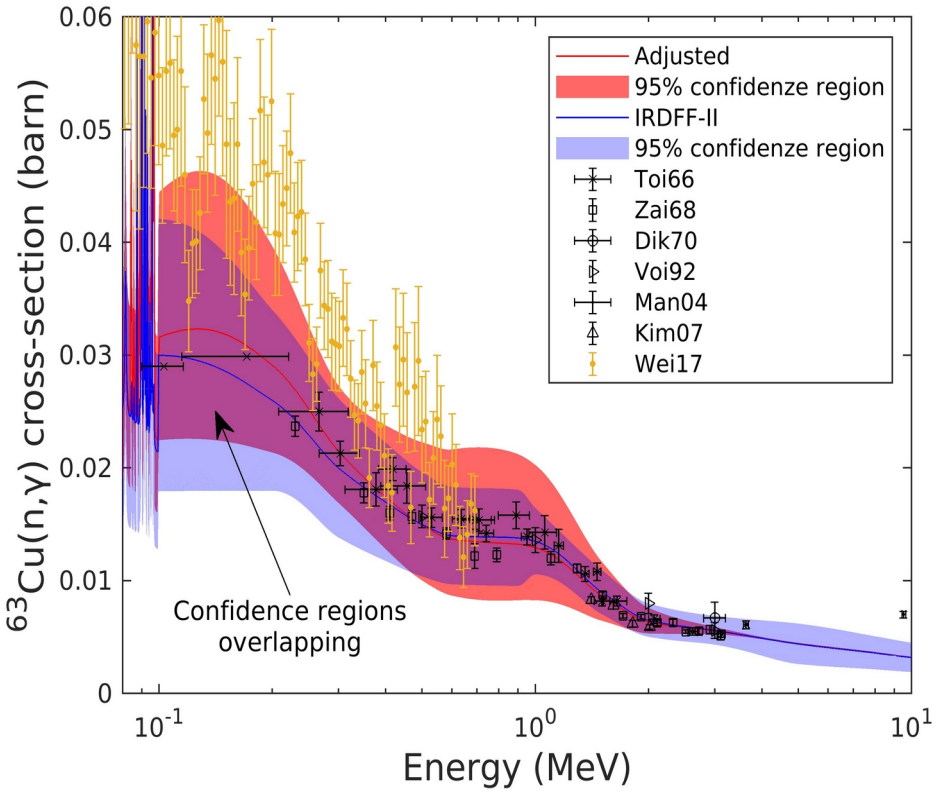

Figure 26: IRDFF-II and adjusted cross-section of the $^{63}Cu(n,\gamma)^{64}Cu$ reaction with the 95% confidence regions compared with the experimental values in the Unresolved Resonance Region.

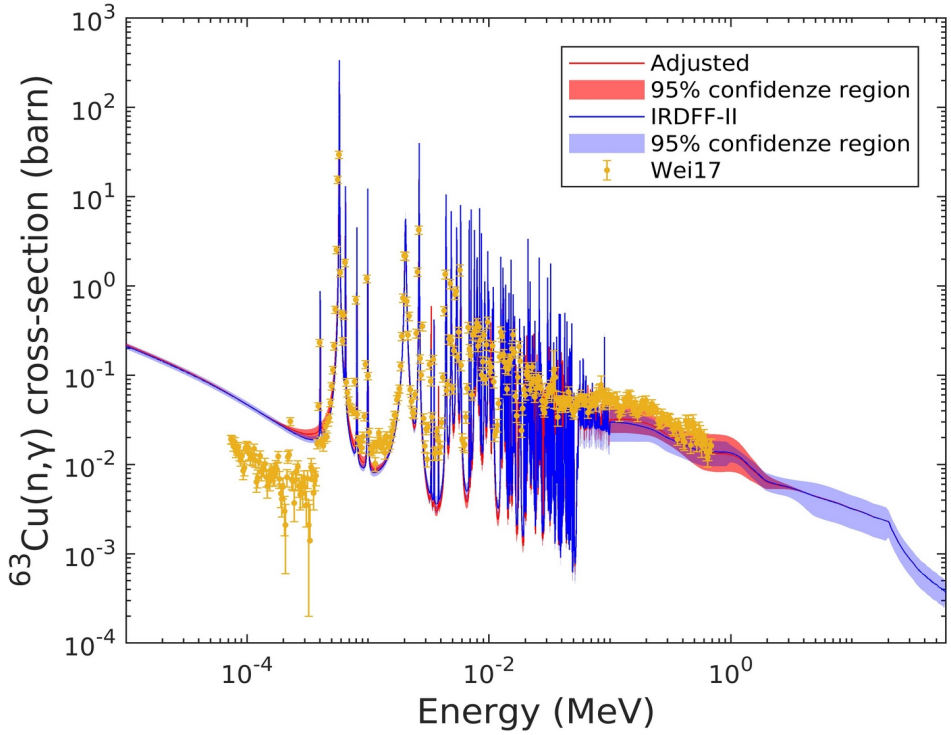

Figure 27: complete set of Wei17 experimental data and IRDFF-II and adjusted $^{63}Cu(n,\gamma)$ cross-sections

The improvement attained with the adjusted cross-section was quantified by calculating the Residual Sum of Square (RSS) between the experimental data σ_i^{exp} measured at the energy E_i and the evaluated/adjusted $\sigma(E_i)$ cross-sections at the same energies:

$$RSS = \sum_i (\sigma_i^{exp} - \sigma(E_i))^2 \tag{49}$$

The RSS was evaluated for all the experimental data reported in Figure 26 and all the points of [61] (Wei17 data). Two distinct calculations were performed with and without the Wei17 data to quantify the improvement obtained with the adjusted cross-sections. Based on the considered experimental data, excluding the Wei17 points, the results of the RSS calculations are reported in Table 16 and indicate that the IRDFF-II cross-section fits the experimental data slightly better than that obtained with the adjusted cross-section. The RSS is 0.0212 barn^2 for the IRDFF-II cross-section against the 0.0229 barn^2, about 8% higher, for the adjusted cross-section. The results are opposite with the inclusion of the Wei17 data, the RSS value, that is 668.8 barn^2 for the IRDFF-II cross-section, becomes 312.1 barn^2 when the adjusted cross-section is considered. This result indicates that the adjusted cross-section is more accurate than the IRDFF-II corss-section when the new data are included in the comparison.

Table 16: residual sum of square evaluated with and without the Wei17 data

RSS (barn^2)		
Cross-section	**Old experimental data**	**Old + Wei17 data**
IRDFF-II	0.0212	668.8
Adjusted (this work)	0.0229	321.1

The propagation of the distributions has made possible the determination of the correlation of the adjusted cross-section energy function. The Monte Carlo algorithm described in Chapter 5 generates, for each energy, a distribution of the cross-section values $\widetilde{\sigma}(E)$ that allows the calculation of the correlation bivariate function:

$$\rho(\widetilde{\sigma}(E), \widetilde{\sigma}(E')) = \frac{\mathrm{cov}(\widetilde{\sigma}(E), \widetilde{\sigma}(E'))}{\sqrt{\mathrm{Var}(\widetilde{\sigma}(E)) \cdot \mathrm{Var}(\widetilde{\sigma}(E'))}} \qquad \forall E, E' \tag{50}$$

The result is shown in Figure 28 for the neutron energies below 10 MeV. The correlation is strongly influenced by the dependence established in the definition of the continuity conditions between the cubic polynomials that define the spline.

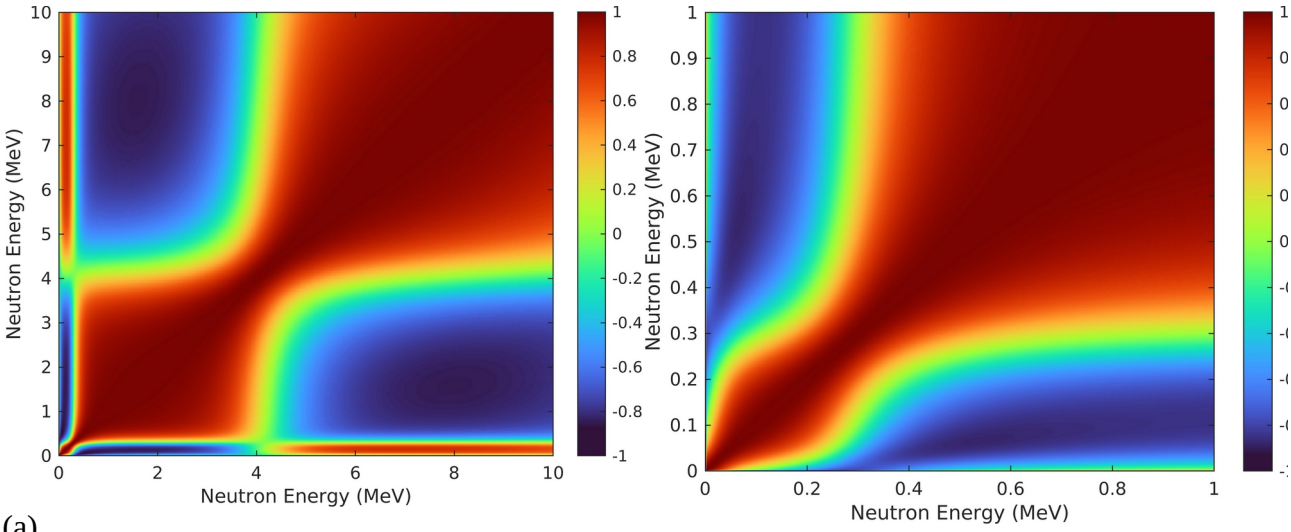

(a) (b)

Figure 28: correlation matrix for the adjusted cross-section: limited to 10 MeV (a) and to 1 MeV (b)

The relative uncertainties of the IRDFF-II and adjusted cross-sections assumes a comparable value in a wide energy range. Figure 29 reports the comparison of the two relative uncertainties showing that in the RRR and in part of the URR regions the two curves are comparable, and in some cases, the uncertainty of the adjusted cross-section is higher than for the *a priori* cross-section. Furthermore, the energy dependence of the adjusted cross-section relative uncertainty shows two tails that go below the relative uncertainty of the *a priori* cross-section because of the energetic limits of the available neutron spectra.

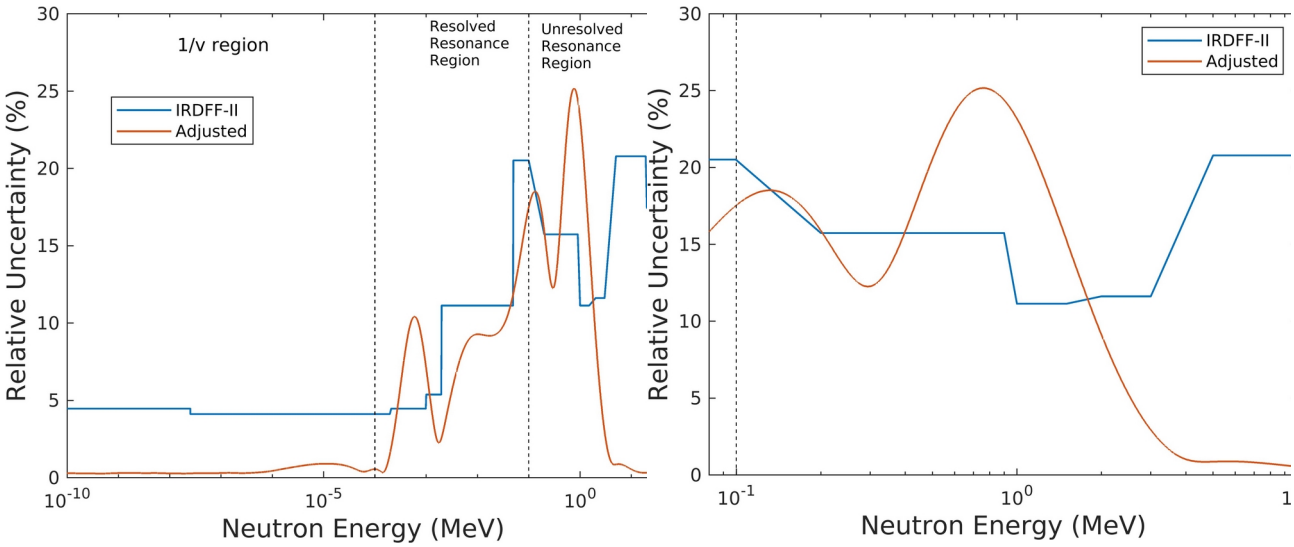

Figure 29: comparison between the relative uncertainty of the IRDFF-II and adjusted ^{63}Cu(n,γ) cross-sections

The analysis of the origins of the total uncertainty reveals that the most important contribution is generated by the uncertainties of the neutron energy spectra. Figure 30 shows the energy dependence of the components of the relative uncertainty of the ^{63}Cu(n,γ) adjusted cross-section compared with the total relative uncertainty of the IRDFF-II cross-section. The relative uncertainty of the neutron energy spectra is greater than the total uncertainty but it should be noted that the statistical relative uncertainties are added in quadrature. The uncertainties of the activities contribute to an amount below 5% and those due to the intrinsic stochastic nature of the algorithm provide a negligible contribution.

Almost the totality of the total uncertainty is then attributable to the neutron energy spectra. But, as a result of the uncertainty analysis reported in paragraph 7.2.3, and in particular in Figure 21, the neutron energy spectra uncertainties are mainly due to the IRDFF-II cross-sections of the reactions ^{59}Co(n,γ)^{60}Co and ^{27}Al(n,α)^{24}Na. In the end, it is, therefore, possible to state that the total relative uncertainty of the ^{63}Cu(n,γ)^{64}Cu cross-section, adjusted by the method introduced in this work, is mainly generated by the evaluated cross-sections.

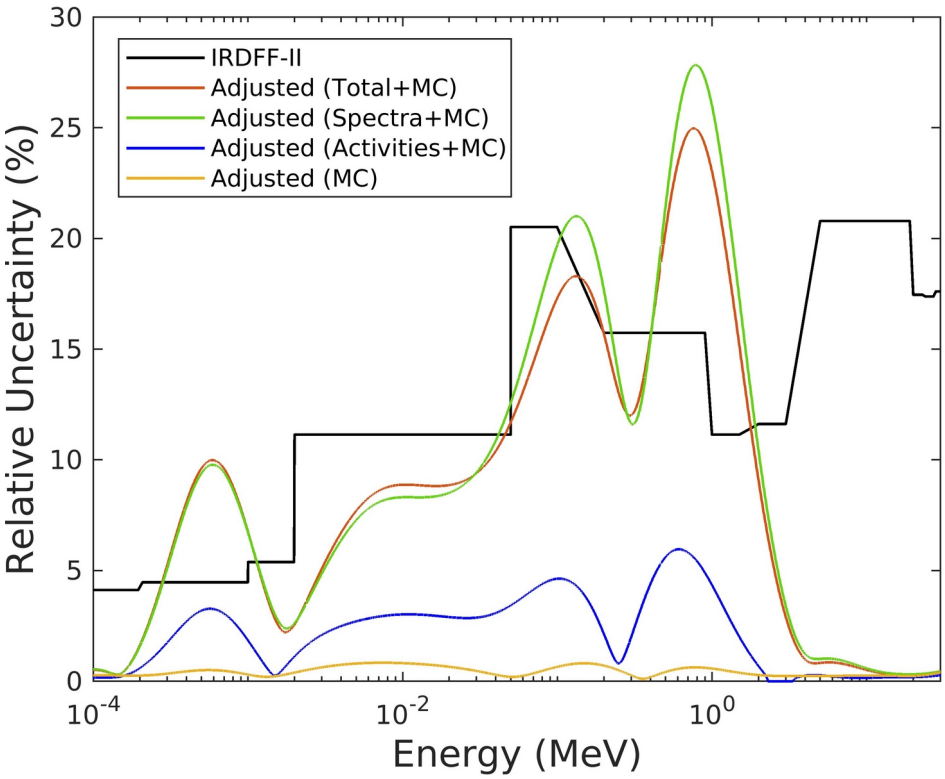

Figure 30: uncertainties components for the adjusted ^{63}Cu(n,γ) cross-sections

8 Future experimental verification

The TAPIRO reactor is involved in an experimental campaign for the measurement of the capture cross-sections of some minor actinides such as neptunium, americium, and curium. The Working Party on Nuclear Criticality Safety (WPNCS) Subgroup on Experimental Needs for Criticality Safety Purposes [62] has identified the TAPIRO reactor with the associated experimental program AOSTA (Activation of OSMOSE Samples in TApiro) as one of the facilities for performing integral experiments. The AOSTA experimental campaign is subdivided into two phases. In the first phase, the properties of the neutron energy distributions in several positions inside the irradiation channels of the reactor are measured utilizing metallic foils (neutron activation) and fission chambers (reaction rates) [37]. In the second phase the neutron activation of the OSMOSE samples, containing minor actinides, will be measured. The experimental data interpretation and elaboration phase includes an adjustment procedure based on a statistical approach in which the likelihood that the model parameters match the experimental integral values, is maximized [63]. The AOSTA experimental campaign could be an opportunity for testing the cross-section adjustment method described in Chapters 3, 4, and 5. Moreover, the neutron energy spectrum adjustment described in paragraph 7.2.1 could be applied in the first phase for determining the neutron energy spectra with the multi-foil activation method and could be compared with the results of the traditional codes like SAND-II and STAY'SL. The application of the proposed adjustment methods could be performed in parallel with the elaborations planned in the AOSTA program.

Dedicated experiments could be designed to extend the range of energies where the proposed cross-section adjustment method is effective. The neutron energy spectrum can be softened with moderating material like Polyethylene. For example, the innermost part of the radial channel 1 (RC1) can be filled with a cylinder of Polyethylene with a diameter of 5.6 cm and a length of 10 cm (see Figure 31a). The MCNP estimation of the neutron energy spectrum in the center of the Polyethylene zone shows a spectrum per unit lethargy similar to that of the thermal reactor with two peaks, one at 0.05 eV and the other at about 0.4 MeV as shown in Figure 31b. The comparison with the neutron spectrum in the RC2/P1 position, the less energetic spectrum considered in this work, clearly shows that the range of neutron energies is much larger.

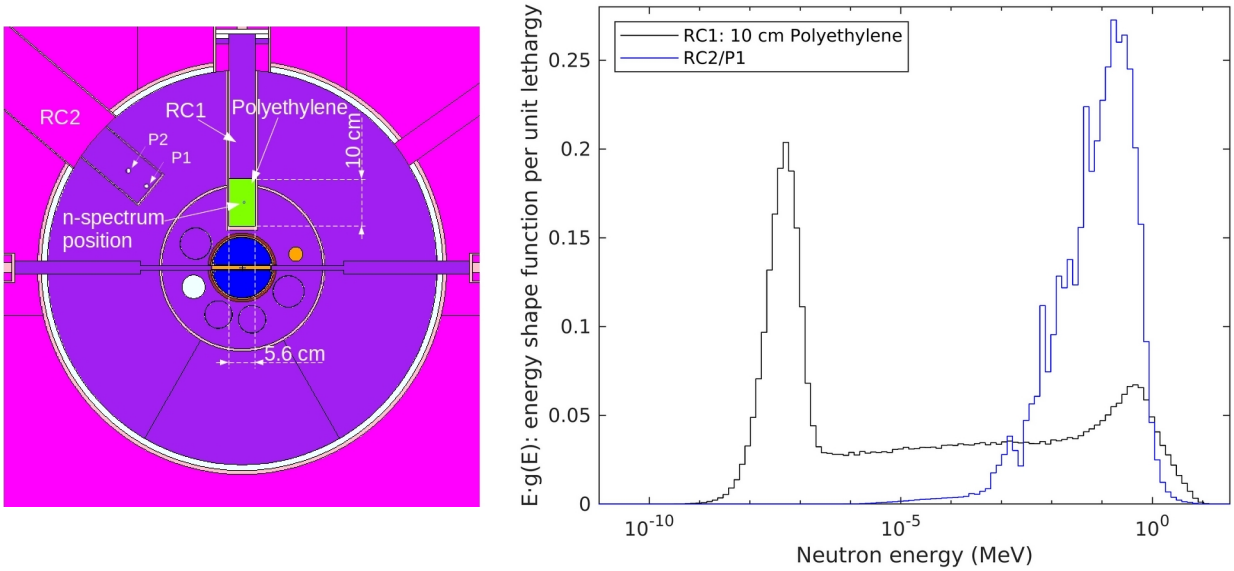

(a) (b)

Figure 31: (a) TAPIRO horizontal section with the position and geometry of the cylinder of Polyethylene in RC1 channel, (b) energy shapes of neutron energy spectra in RC2/P1 (blue line) and in the center of 10 cm length cylinder of Polyethylene in RC1 (black line)

Additional measurement positions can be arranged in the Polyethylene cylinder obtaining neutron energy spectra with different energy ranges. The purpose is to have several measurement positions with the widest possible variety of neutron energy spectra and different solutions can be investigated with the utilization of different types of materials that act as neutron “energy filters”.

A final consideration must be accounted for in the list of reactions considered in the application of the multi-foil activity technique. The list should include reactions with as accurate as possible evaluated cross-sections and low uncertainties. The measurement of the neutron activities should be properly corrected for systematic errors and avoid the typical experimental effects like self-shielding and coincidence summing. A list of reactions in thermal and fast neutron regions can be found in [64]. The reactions that are measurable in the TAPIRO reactor because compatible with the operation procedure, for example the time for removing the irradiated sample from the channel, and the available instrumentation are reported in Table 17.

Table 17: list of reactions that can be considered for the application of the multi-foil activation technique at the TAPIRO reactor.

$^{27}Al(n,\alpha)^{24}Na$	$^{115}In(n,\gamma)^{116m}In$
$^{27}Al(n,p)^{27}Mg$	$^{115}In(n,n')^{115m}In$
$^{197}Au(n,\gamma)^{198}Au$	$^{58}Ni(n,p)^{58}Co$
$^{59}Co(n,\alpha)^{56}Mn$	$^{46}Ti(n,p)^{46}Sc$
$^{59}Co(n,\gamma)^{60}Co$	$^{47}Ti(n,p)^{47}Sc$
$^{63}Cu(n,\gamma)^{64}Cu$	$^{48}Ti(n,p)^{48}Sc$
$^{56}Fe(n,p)^{56}Mn$	$^{64}Zn(n,p)^{64}Cu$
$^{54}Fe(n,p)^{54}Mn$	

9 Conclusions and final remarks

The mathematical relation on which it is based on the multi-foil activation technique for the determination of the neutron energy spectrum, namely the relation (5), was adopted for developing a new method for adjusting a continue-energy cross-section. By being derived from the multi-foil activation technique, the method proposed for the adjustment of cross-section can be applied to the same reactions. But, in contrast to the multi-foil activation technique, where foils of different materials must be irradiated in the same neutron spectrum, in this method, several foils of the same material must be irradiated in different neutron energy spectra.

The neutron activation of the foils and the neutron energy spectra in different experimental positions are the known quantities of the set of integral equations where the cross-section function is the unknown quantity to be determined (see equations 7). Unfortunately, the mathematical representation of the problem provides an ill-posed system of integral equations because the solution of this system is not unique. However, an algorithm is proposed for the determination of a possible solution obtained as an adjustment of the evaluated cross-section (*a priori* cross-section) obtained from one of the freely available nuclear data libraries. The main characteristics of the algorithm are:

- a continue-energy adjustment is performed interpolating the cross-section energy function with a cubic spline. The continuity conditions, that uniquely define the cubic spline, introduce a correlation in the energy dependence of the adjusted cross-section;
- the cost function is defined as the sum of squares of the relative errors between the calculated and experimental activities;
- the adjusted cross-section is obtained minimizing the cost function with the implementation of the stochastic hill-climbing optimization method. This method provides a local minimum, that is the solution closer to the *a priori* cross-section;
- the experimental uncertainties of the saturated activities and neutron energy spectra are propagated making use of the Monte Carlo technique. The application of the traditional second-order approximation of the Taylor series is impracticable.

The algorithm was implemented in GNU Octave high-level language and tested on the $^{63}Cu(n,\gamma)^{64}Cu$ cross-sections utilizing the activities and neutron spectra measured in different positions inside the irradiation channel of the RSV TAPIRO fast neutron source reactor.

The TAPIRO inoperability that occurred in the last year has not allowed the execution of dedicated experiments and has forced seeking, among the old experiments performed at TAPIRO, some useful data. In the measurements performed by A. Fabry from 1983 to 1987 were found the minimal data needed for testing the algorithm on the $^{63}Cu(n,\gamma)^{64}Cu$ cross-sections. The activation of the $^{63}Cu(n,\gamma)^{64}Cu$, $^{59}Co(n,\gamma)^{60}Co$, and $^{27}Al(n,\alpha)^{24}Na$ reactions were measured by Fabry in eight experimental positions in the same power and reactor configuration.

However, Fabry did not provide the neutron energy spectra in the eight positions that, therefore, were determined using the multi-foil activation technique with the activities of the $^{59}Co(n,\gamma)$, and $^{27}Al(n,\alpha)$ reactions, although they constitute a very meager number of observations.

The continue-energy adjustment of the cross-section requires neutron spectra in the form of continue-energy functions and an adequate uncertainty propagation algorithm. For these reasons, a new algorithm was implemented to overcome the limits of the commonly adjusted codes that make use of energy groups and only a few of them perform the propagation of the uncertainties. The new algorithm takes advantage of the characteristics of the algorithm implemented for the cross-section adjustment, although it requires to be validated through a comparison with the certified codes on specific benchmark cases. As for all the adjusted codes, the new neutron spectrum adjustment algorithm makes use of an *a priori* neutron energy spectrum and a cost function to be minimized. The *a priori* neutron energy spectra were determined with the MCNP code modifying the validate model of the TAPIRO adding the neutron energy spectra estimators (tally type F4) in the experimental positions examined by Fabry. Subsequently, the MCNP results were interpolated with cubic splines to have continuous energy functions. A revised cost function was introduced to limit the possible predominance of some reactions in the numerical minimization.

The eight neutron energy spectra were determined with an extremely good agreement between calculated and experimental values of the saturated activities per target nucleus. Excluding the position P6 inside side B of the tangential channel of the TAPIRO reactor, where the calculation-experiment relative error is 2.5%, the other differences are below 0.16% for both the $^{59}Co(n,\gamma)$ and $^{27}Al(n,\alpha)$ reactions. The improvement with respect to the activities calculated with the *a priori*

spectra (splines of the MCNP results) is significant, excluding the TCB/P6 position where the relative error is reduced by half, in the other positions the relative errors are at least 31 times lower.

The propagation of the uncertainties was carried out supposing a normal distribution for the experimental data and 528 sampling for each probability density function. The calculations were executed on the CRESCO scientific computing infrastructure using 11 nodes each one with 48 CPUs. The propagation algorithm provided the probability density function of the neutron energy differential flux for each energy. From the resulting sample were estimated the main statistical quantities of the probability density functions. The statistical relative errors of the calculated saturated activities per target nucleus are practically unchanged with respect to the experimental uncertainties. The mean neutron energy spectra and the 95% confidence regions were determined.

The total uncertainty has three components originated by: the experimental uncertainties of the measured saturated activities per target nucleus; the evaluated cross-sections; and the intrinsic stochastic nature of the adjustment algorithm. The analysis of the origin of the uncertainties of the neutron energy spectra reveals that the predominant components are attributable to the evaluated cross-sections of the ^{59}Co(n,γ) and ^{27}Al(n,α) reactions. On the contrary, the uncertainties of the saturated activities are mainly originated by the experimental uncertainties of the saturated activities. The intrinsic stochastic error component is lower than the other and generally negligible.

Once the neutron energy spectra were determined, the cross-section adjustment algorithm was applied to the ^{63}Cu(n,γ)^{64}Cu energy-dependent cross-section. The experimental position TCB/P6 was not included in the cross-section adjustment because of the high calculation vs. experiment relative uncertainty. An investigation into the origin of these discrepancies with respect to the other data will be carried out in future work.

The *a priori* ^{63}Cu(n,γ) cross-section was extracted by the International Reactor Dosimetry and Fusion File IRDFF-II cross-sections currently available. Although the library was updated in 2020, the cross-section data of the ^{63}Cu(n,γ) reaction refer to the old IRDF-2002 file for the neutron energies between thermal to 20 MeV and the TENDL-2011 library for energies from 20 MeV to 60 MeV.

Before the adjustment, all the calculated activities overestimated the experiment by, on average, the 3.5% and with a minimum of 2.17%. After the adjustment, the absolute calculated vs.

experimental relative difference is at a maximum of 0.64% with an improvement with respect to the original IRDFF-II cross-section of an order of magnitude before the adjustment.

The ^{63}Cu(n,γ) adjusted and IRDFF-II cross-sections differ in the resolved and unresolved resonance regions whereas are practically equal in the $1/v$ energy region. Although the differences are minimal, excluding the $1/v$ region, the cross-section adjustment procedure has produced an average increment of the cross-section in the unresolved region and a reduction in the resolved resonance region.

The propagation of the uncertainty indicates that the adjusted cross-section maintains the same uncertainty level as the a priori IRDFF-II cross-section and no improvements are achieved for the precision of the data. The maximum value of 25% of the statistical relative error is reached in the unresolved resonance region against the 20% of the IRDFF-II cross-section. The uncertainties analysis reveals that the uncertainties of the neutron energy spectra are nearly the totality of the total cross-section uncertainties. On the other hand, the neutron spectra uncertainties, as aforesaid, are mainly due to the uncertainties on the IRDFF-II evaluated ^{59}Co(n,γ)^{60}Co and ^{27}Al(n,α)^{24}Na cross-sections. It may therefore be concluded that the main origin of the final cross-section uncertainties resides in the evaluated nuclear data.

A considerable improvement in the accuracy was reached by comparing the adjusted cross-section result with the new time-of-flight experimental data, carried out in 2017, then after the IRDFF-II evaluation of the ^{63}Cu(n,γ) reaction. The Residual Sum of Squares (RSS), calculated with respect to the old (data taken before the 2017) experimental data, assumes the 0.0212 barn^2 value when the IRDFF-II cross-section is considered, and the 0.0229 barn^2 for the adjusted cross-section. The IRDFF-II cross-section provides a better agreement, although the difference between the two values is minimal. But, when the new 2017 experimental data are considered, the situation is reversed, the RSS goes from 668.8 barn^2 for the original IRDFF-II to 321.1 barn^2, the half, for the adjusted cross-section.

The measurements carried out at the TAPIRO reactor have provided a sufficient, even if minimal, number of experimental positions for a preliminary test of the method on the ^{63}Cu(n,γ) reaction in the resolved and unresolved energy range. New measurements, with additional experimental positions and reactions, could be useful for validating the proposed method in different energy ranges and reducing the total uncertainties.

In conclusion, the proposed method could be promising support for validating and adjusting the available evaluated energy-dependent cross-sections by using the “local” integral experimental data regarding the neutron activation measurements. The method is limited to the type of reactions normally considered in the multi-foil activation analysis. The uncertainties are strongly dependent on the neutron energy spectra uncertainties. If the multi-foil activation technique is utilized for the neutron energy spectra measurement, particular attention must be paid to the cross-section uncertainties of the chosen reactions. The TAPIRO reactor could be a valid source of neutrons for testing this method in different ranges of energies below the typical energy of 20 MeV considered in the nuclear reactor.

10 Appendix A

Table 18: upper boundaries of the energies in MeV intervals for the flux estimation. (the lowest boundary is 0 MeV)

N.	Energy (MeV)	N.	Energy (MeV)	N.	Energy (MeV)	N.	Energy (MeV)
1	1.000E-11	28	2.060E-07	55	1.760E-04	82	1.500E-01
2	3.090E-10	29	2.640E-07	56	2.250E-04	83	1.930E-01
3	3.970E-10	30	3.390E-07	57	2.900E-04	84	2.470E-01
4	5.100E-10	31	4.350E-07	58	3.720E-04	85	3.180E-01
5	6.540E-10	32	5.590E-07	59	4.770E-04	86	4.080E-01
6	8.400E-10	33	7.180E-07	60	6.130E-04	87	5.230E-01
7	1.080E-09	34	9.210E-07	61	7.870E-04	88	6.720E-01
8	1.390E-09	35	1.180E-06	62	1.010E-03	89	8.630E-01
9	1.780E-09	36	1.520E-06	63	1.300E-03	90	1.110E+00
10	2.280E-09	37	1.950E-06	64	1.670E-03	91	1.420E+00
11	2.930E-09	38	2.510E-06	65	2.140E-03	92	1.830E+00
12	3.770E-09	39	3.220E-06	66	2.750E-03	93	2.350E+00
13	4.840E-09	40	4.130E-06	67	3.530E-03	94	3.010E+00
14	6.210E-09	41	5.300E-06	68	4.530E-03	95	3.870E+00
15	7.970E-09	42	6.810E-06	69	5.810E-03	96	4.970E+00
16	1.020E-08	43	8.740E-06	70	7.470E-03	97	6.380E+00
17	1.310E-08	44	1.120E-05	71	9.590E-03	98	8.190E+00
18	1.690E-08	45	1.440E-05	72	1.230E-02	99	1.050E+01
19	2.170E-08	46	1.850E-05	73	1.580E-02	100	1.350E+01
20	2.780E-08	47	2.380E-05	74	2.030E-02	101	1.730E+01
21	3.570E-08	48	3.050E-05	75	2.610E-02	102	2.000E+01
22	4.590E-08	49	3.920E-05	76	3.350E-02	103	3.000E+01
23	5.890E-08	50	5.030E-05	77	4.300E-02	104	3.100E+01
24	7.560E-08	51	6.460E-05	78	5.520E-02	105	3.200E+01
25	9.710E-08	52	8.290E-05	79	7.080E-02	106	3.300E+01
26	1.250E-07	53	1.070E-04	80	9.100E-02	107	3.400E+01
27	1.600E-07	54	1.370E-04	81	1.170E-01	108	3.500E+01

References

[1] K. Kolos, V. Sobes, R. Vogt , C.E. Romano, M.S. Smith, L.A. Bernstein, D.A. Brown, M.T. Burkey, Y. Danon, M.A. Elsawi, et al.. Current nuclear data needs for applications, Phys. Rev. Res., Volume 4, Issue 2, 2022, American Physical Society, doi:10.1103/PhysRevResearch.4.021001.

[2] NEA Nuclear Data High Priority Request List, HPRL. <https://www.oecd-nea.org/dbdata/hprl/hprlview.pl?ID=477>, 2023 (accessed 28.10.23).

[3] Nuclear Criticality Safety Program, U.S. Department of Energy. <https://ncsp.llnl.gov/>, 2023 (accessed 28.10.23).

[4] Five Year Execution Plan – for the Mission and Vision of the United States Department of Energy Nuclear Criticality Safety Program FY 2023 through FY 2027, August 2022. <https://ncsp.llnl.gov/sites/ncsp/files/2022-08/ncsp_five-year_execution_plan_fy2023-2027_-_final.pdf>, 2023 (accessed 28.10.23).

[5] P. Romojaro, F. Álvarez-Velarde, O. Cabellos, N. García-Herranz, A. Jiménez-Carrascosa, On the importance of target accuracy assessments and data assimilation for the co-development of nuclear data and fast reactors: MYRRHA and ESFR, Annals of Nuclear Energy, Volume 161, 2021, ISSN 0306-4549, doi:10.1016/j.anucene.2021.108416.

[6] R.C. Block, Y. Danon, F. Gunsing, R.C. Haight, Neutron Cross Section Measurements, in: D.G. Cacuci (Ed.) Handbook of Nuclear Engineering, Springer, Boston, MA, 2010, doi:10.1007/978-0-387-98149-9_1.

[7] n_TOF. The neutron time-of-flight facility at CERN. <https://ntof-exp.web.cern.ch/index.php?page=main>, 2023 (accessed 28.10.23).

[8] G. Palmiotti, M. Salvatores, Revisiting the bias factor methodologies for the validation of fast test reactors, Annals of Nuclear Energy, Volume 145. 2020, doi:10.1016/j.anucene.2020.107591.

[9] L.N. Usachev, Y. Bobkov, Planning an optimum set of microscopic experiments and evaluations to obtain a given accuracy in reactor parameter calculations, Report INDC(CCP)-19/U, IAEA International Data Committee, January 1972.

[10] U. Farinelli, The role of integral data, Report RT/FI(73)28, Comitato Nazionale Energia Nucleare, 1973.

[11] Assessment of Existing Nuclear Data Adjustment Methodologies, International Evaluation Cooperation, Intermediate Report of WPEC Subgroup 33, NEA/NSC/WPEC/DOC(2010)429, OECD/NEA, Paris, 2011.

[12] M. Salvatores, G. Palmiotti, G. Aliberti, P. Archier, C. De Saint Jean, E. Dupont, M. Herman, M. Ishikawa, T. Ivanova, E. Ivanov, et al., Methods and Issues for the Combined Use of Integral Experiments and Covariance Data: Results of a NEA International Collaborative Study, Nuclear Data Sheets, Volume 118, 2014, pp. 38-71, ISSN 0090-3752, doi:10.1016/j.nds.2014.04.005.

[13] A. Koning, S. Hilaire, S. Goriely, TALYS: modeling of nuclear reactions, Eur. Phys. J. A 59, 131 (2023), doi:doi.org/10.1140/epja/s10050-023-01034-3.

[14] U. Farinelli, Nuclear data and integral experiments in reactor physics, IAEA-SMR-44, pp. 17-39, 1980.

[15] G. Palmiotti, M. Salvatores, Cross section covariances: a user perspective, EPJ Nuclear Sci. Technol., 4 (2018) 40, Published online: 2018-11-14, doi:10.1051/epjn/2018021.

[16] M. Matzke, Unfolding procedures, Radiation Protection Dosimetry Radiat Prot Dosimetry, Volume 107, Issue 1-3, 2003, pp. 155-174, doi: 10.1093/oxfordjournals.rpd.a006384.

[17] M. Reginatto, Overview of spectral unfolding techniques and uncertainty estimation, Radiation Measurements, Volume 45, Issue 10, 2010, pp. 1323-1329, ISSN 1350-4487, doi:10.1016/j.radmeas.2010.06.016.

[18] A. Trkov, P.J. Griffin, S.P. Simakov, L.R. Greenwood, K.I. Zolotarev, R. Capote, D.L. Aldama, V. Chechev, C. Destouches, A.C. Kahler, et al., IRDFF-II: A New Neutron Metrology Library, Nuclear Data Sheets, Volume 163, 2020, ISSN 0090-3752, doi:10.1016/j.nds.2019.12.001.

[19] A.J. M. Plompen, O. Cabellos, C. De Saint Jean, M. Fleming, A. Algora, M. Angelone, P. Archier, E. Bauge, O. Bersillon, A. Blokhin, et al.,The joint evaluated fission and fusion nuclear data library, JEFF-3.3, Eur. Phys. J. A 56 (7) (2020) 181, doi:10.1140/epja/s10050-020-00141-9.

[20] D.A. Brown, M.B. Chadwick, R. Capote, A.C. Kahler, A. Trkov, M.W. Herman, A.A. Sonzogni, Y. Danon, A.D. Carlson, M. Dunn, at al., ENDF/B-VIII.0: The 8th Major Release of the Nuclear Reaction Data Library with CIELO-project Cross Sections, New Standards and Thermal Scattering Data, Nuclear Data Sheets, Volume 148, 2018, pp. 1-142, ISSN 0090-3752, doi:10.1016/j.nds.2018.02.001.

[21] Nuclear Data Center. Japan Atomic Energy Agency, <https://wwwndc.jaea.go.jp/index.html>, 2023 (accessed 28.10.23).

[22] T. Weise. An Introduction to Optimization Algorithms, Institute of Applied Optimization (IAO) of the School of Artificial Intelligence and Big Data of Hefei University, Hefei, Anhui, China, 2020.

[23] H.H. Hoos, T. Stützle, Stochastic Local Search, A volume in The Morgan Kaufmann Series in Artificial Intelligence, 2005, doi:10.1016/B978-1-55860-872-6.X5016-1.

[24] S.J. Russell, P. Norvig, Artificial Intelligence: A Modern Approach, 2nd ed. Prentice Hall, Upper Saddle River, NJ, 2002, ISBN: 0-1379-0395-2.

[25] T. Weise, Global Optimization Algorithms - Theory and Application, 2009. <http://www2.fiit.stuba.sk/~kvasnicka/Free%20books/Weisse_Global%20Optimization%20Algorithms%20-%20Theory%20and%20Application.pdf>, 2023 (accessed 28.10.23).

[26] J.C. Spall, Introduction to Stochastic Search and Optimization. Estimation, Simulation and Control. Wiley-Interscience Series in Discrete Mathematics and Optimization. John Wiley & Sons, first edition, June 2003, p. 618.

[27] J.W. Eaton, D. Bateman, S. Hauberg, R. Wehbring, GNU Octave version 5.1.0 manual: a high-level interactive language for numerical computations, 2019. Available from: https://www.gnu.org/software/octave/doc/v5.2.0/

[28] F. Iannone, F. Ambrosino, G. Bracco, M. De Rosa, A. Funel, G. Guarnieri, S. Migliori, F. Palombi, G. Ponti, G. Santomauro, et al., CRESCO ENEA HPC clusters: a working example of a multifabric GPFS Spectrum Scale layout, 2019 International Conference on High Performance Computing & Simulation (HPCS), Dublin, Ireland, 2019, pp. 1051-1052, doi:10.1109/HPCS48598.2019.9188135

[29] M. Matsumoto, T. Nishimura, Mersenne Twister: A 623-dimensionally equidistributed uniform pseudorandom number generator, ACM Trans. on Modeling and Computer Simulation Vol. 8, No. 1, January 1998, pp. 3–30.

[30] W.M. Gentleman, Implementing Clenshaw-Curtis quadrature I: Methodology and experience, Communications of the ACM 15(5), p. 337-342 (1972).

[31] BIPM, IEC, IFCC, ILAC, ISO, IUPAC, IUPAP, and OIML. Evaluation of measurement data - Supplement 1 to the “Guide to the expression of uncertainty in measurement” - Propagation of distributions using a Monte Carlo method. Joint Committee for Guides in Metrology, JCGM, 2008. Available from: https://www.bipm.org/en/committees/jc/jcgm/publications.

[32] R. Zona, G. Rosi, A. Santagata, Breve storia del "TAPIRO", ENEA report RT/2021/10/ENEA, 2021, <https://iris.enea.it/retrieve/dd11e37c-fb46-5d97-e053-d805fe0a6f04/ENEA-RT-2021-10.pdf>, 2023 (accessed 28.10.23).

[33] M. Cesaroni, B. Bianchi, A. Dodaro, A. Ratto, P. Ricci, A. Rosada, A. Santagata, Contribution to IAEA Research Reactors Catalogue - ENEA RSV TAPIRO Reactor, ENEA report UTFISST-REANUC/RT/002, December 2013.

[34] ASIF (ASI SUpported Irradiation Facilities), <http://www.asif.asi.it/index.php/asif-facilities/tapiro-at-casaccia>, 2023 (accessed 28.10.23).

[35] M. Angelone, A. Klix, M. Pillon, P. Batistoni, U. Fischer, A. Santagata, Development of self-powered neutron detectors for neutron flux monitoring in HCLL and HCPB ITER-TBM, Fusion Engineering and Design, Volume 89, Issues 9–10, 2014, Pages 2194-2198, ISSN 0920-3796, doi:10.1016/j.fusengdes.2014.01.077.

[36] M. Pillon, C. Monti, G. Mugnaini, C. Neri, P. Rossi, M. Carta, O. Fiorani, A. Santagata, Study of the response of a piezoceramic motor irradiated in a fast reactor up to a neutron fluence of 2.77E+17n/cm2, Fusion Engineering and Design, Volumes 96–97, 2015, Pages 329-333, ISSN 0920-3796, doi:10.1016/j.fusengdes.2015.03.025.

[37] V. Fabrizio, M. Carta, M. Cesaroni, L. Falconi, A. Grossi, A. Santagata, P. Blaise, B. Geslot, Neutron characterization of the TAPIRO fast neutron source reactor after the restoring of the nominal configuration, in: Proceedings of ICRR – International Conference on Research Reactors: Addressing Challenges and Opportunities to Ensure Effectiveness and Sustainability, Buenos Aires, Argentina, 25-29 November 2019, IAEA, Vienna (Austria), December 2020, ISBN 978-92-0-131820-6.

[38] S. Abovyan, B. Bianchi, M. Cesaroni, M. Corradi, V. Danielyan, L. Falconi, R. Ferraro, M. Fras, P. Gkountoumis, O. Kortner, H. Kroha, I. Longarini, R. Lunadei, A. Ratto, P. Ricci, R. Richter, S. Rosati, A. Santagata, R. Vari, Test of low-dropout voltage regulators with neutrons and protons, Journal of Instrumentation, Volume 17, May 2022, doi:10.1088/1748-0221/17/05/C05006.

[39] A. D'Angelo, M. Martini, M. Salvatores, The TAPIRO fast source reactor as a benchmark for nuclear data testing, CNEN report RT/FI(74)7, Comitato Nazionale per l'Energia Nucleare, 1974.

[40] P. Pihet, M. Coppola, T. Loncol, V. Di Majo, H.G. Menzel, Microdosimetry Study of Radiobiological Facilities at the RSV - TAPIRO Reactor, Radiation Protection Dosimetry, Volume 52, Issues 1-4, 1994, Pages 409-414, doi:10.1093/oxfordjournals.rpd.a082224.

[41] Argonne Fast Source Reactor, <https://www.youtube.com/watch?v=aXuJTTrQYIU>, 2023 (accessed 28.10.23).

[42] ASTM Standard E722, Standard Practice for Characterizing Neutron Energy Fluence Spectra in Terms of an Equivalent Monoenergetic Neutron Fluence for Radiation-Hardness Testing of Electronics, ASTM International, West Conshohocken, PA, 2019, doi:10.1520/E0722-19.

[43] A. Fabry, Neutronic Characterization of the TAPIRO Fast-Neutrons Source Reactor - Final Report, vols. 1–4, 1986. . Available from: http://www.oecd-nea.org/tools/abstract/detail/nea-1764.

[44] I. Newsome, M. Bhike, Krishichayan, and W. Tornow, Neutron radiative capture cross-section of ^{63,65}Cu between 0.4 and 7.5 MeV, Physical Review C 97, 044617 (2018), doi:10.1103/PhysRevC.97.044617

[45] J.B. Trice, Techniques for Measuring Reactor Neutron Spectra, Third Pacific Area National Meeting, ASTM (1959), doi:10.1520/STP39584S.

[46] ASTM Standard E261, Standard Practice for Determining Neutron Fluence, Fluence Rate, and Spectra by Radioactivation Techniques, ASTM International, West Conshohocken, PA, 2021, doi:10.1520/E0261-16R21.

[47] F.G. Perey, Least-Squares Dosimetry Unfolding: The Program STAY'SL, Report ORNL/TM-6062, Oak Ridge National Laboratory, Tennessee, October 1977.

[48] R.E. Maerker, B.L. Broadhead, J.J. Wagschal, Theory of a New Unfolding Procedure in Pressurized Water Reactor Pressure Vessel Dosimetry and Development of an Associated Benchmark Data Base, Nucl. Sci. Eng. 91 (2) (1986) 137-170.

[49] M. Tichy, The DIFBAS Program, Description and Users Guide, PTB report PTB-7.2-1993-1, Physikalisch-Technische Bundesanstalt, Braunschweig, 1993.

[50] M. Matzke, Unfolding of Pulse Height Spectra: The HEPRO Program System, Report PTB-N-19, Physikalisch-Technische Bundesanstalt, Braunschweig, 1994.

[51] W.N. McElroy, S. Berg, T. Crockett, and R.G. Hawkins, A Computer-Automated Iterative Method for Neutron Flux Spectra Determination by Foil Activation - Vol. I: A Study of the Iterative Method, Report AFWL-TR-67-41, Air Force Weapons Laboratory, New Mexico, September 1967.

[52] J.G. Kelly, Neutron Spectrum Adjustment with SAND-II Using Arbitrary Trial Functions Reactor, in: Harry Farrar IV and E.P. Lippincott (Eds.), Dosimetry: Methods, Applications, and Standardization, ASTM STP 1001, American Society for Testing & Materials, Philadelphia pp. 460-468 (1989).

[53] J.T. Routti, J.V. Sandberg, General purpose unfolding program LOUHI78 with linear and nonlinear regularizations, Computer Physics Communications, Comput. Phys. Commun. Volume 21, Issues 1, 1980, pp. 119–144, doi: 10.1016/0010-4655(80)90081-8.

[54] E.T. Jaynes, Information Theory and Statistical Mechanics, American Physical Society, Physical Review, Volume 106, Issue 4, May 1957, pp. 620-630, doi:10.1103/PhysRev.106.620

[55] C.J. Werner, J.C. Armstrong, F.B. Brown, J.S. Bull, L. Casswell, L.J. Cox, D.A. Dixon, R.A. Forster III, J.T. Goorley, H.G. Hughes III, et al.,MCNP User's Manual Code Version 6.2. Los Alamos National Laboratory Tech. Rep. LA-UR-17-29981. Los Alamos, NM, USA, October 2017.

[56] N. Burgio, L. Cretara, M. Frullini, A. Gandini, V. Peluso, A. Santagata, Monte Carlo simulation analysis of integral data measured in the SCK-CEN/ENEA experimental campaign on the

TAPIRO fast reactor. Experimental and calculated data comparison, Nuclear Engineering and Design, Volume 273, 2014, pp. 350-358, doi:10.1016/j.nucengdes.2014.03.040.

[57] International Reactor Dosimetry and Fusion File, IRDFF-II, January 2020, <https://www-nds.iaea.org/IRDFF/>, 2023 (accessed 28.10.23).

[58] A.J. Koning, D. Rochman, J. Kopecky, J.Ch. Sublet, M. Fleming, E. Bauge, S. Hilaire, P. Romain, B. Morillon, H. Duarte, et al., TENDL2015: TALYS-based evaluated nuclear data library, 18 January 2016. Available from: https://tendl.web.psi.ch/tendl_2015/tendl2015.html.

[59] V.A. Tolstikov, V.P. Koroleva, V. E. Kolesov, A.G. Dovbenko, Fast neutron radiative capture in ^{63}Cu, Atomnaya Energiya 21, 45 (1966).

[60] G. G. Zaikin, I. A. Korzh, N. T. Sklyar, and I. A. Totskii, Cross sections for radiative capture of fast neutrons by ^{63}Cu, ^{65}Cu, and ^{186}W, Sov. At. Energy 25, 1362 (1968)

[61] M. Diksic, P. Strohal, G. Peto, P. Bornemisza-Pauspertl, I. Hunyadi, and J. Karolyi, Additional measurements of the radiative capture cross sections for 3-mev neutrons, Acta Physica Hungarica 28, 257 (1970).

[62] J. Voignier, S. Joly, G. Grenier, Capture cross sections and gamma-ray spectra from the interaction of 0.5 to 3.0 MeV neutron with nuclei in the mass range A=63 to 209, J. Nucl. Sci. Eng. 112, 87 (1992).

[63] W. Mannhart, D. Schmidt, Measurement of neutron activation cross sections in the energy range from 8 MeV to 15 MeV, AIP Conf. Proc. 769, 609 (2005).

[64] G. D. Kim, H. J. Woo, H. W. Choi, N. B. Kim, T. K. Yang, J. H. Chang, and K. S. Park, Measurements of fast neutron capture cross sections on ^{63}Cu and ^{186}W, J. Radiol. Nucl. Chem. 271, 553 (2007).

[65] M. Weigand, C. Beinrucker, A. Couture, S. Fiebiger, M. Fonseca, K. Göbel, M. Heftrich, T. Heftrich, M. Jandel, F. Käppeler, et al., $^{63}\mathrm{Cu}(n,\gamma)$ cross section measured via 25 keV activation and time of flight, Phys. Rev. C 95, 015808 (2017).

[66] Experimental Needs for Criticality Safety Purposes, Report NEA/NSC/R(2022)6, Nuclear Energy Agency, September 2023. Available from: <https://www.oecd-nea.org/jcms/pl_85234/experimental-needs-for-criticality-safety-purposes>.

[67] M. Carta, V. Fabrizio, A. Grossi, V. Peluso, D. Caron, S. Dulla, P. Ravetto, Assessment of a cross section adjustment formalism using experimental data from the TAPIRO reactor, Report RdS/PAR2015/027, Settembre 2016.

[68] ASTM Standard E720, Standard Guide for Selection and Use of Neutron Sensors for Determining Neutron Spectra Employed in Radiation-Hardness Testing of Electronics, ASTM International, West Conshohocken, PA, 2017, doi:10.1520/E0720-11.